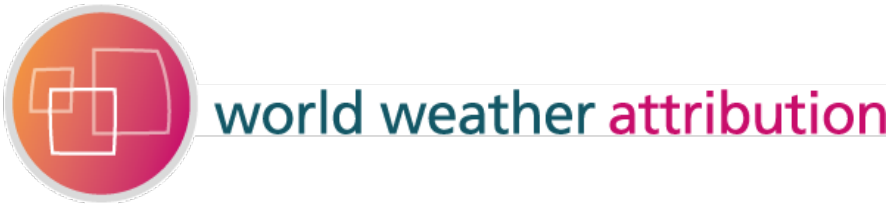

High temperatures exacerbated by climate change made 2022 Northern Hemisphere soil moisture droughts more likely

Dominik L. Schumacher[1], Mariam Zachariah[2], Friederike Otto[2], Clair Barnes[2], Sjoukje Philip[3], Sarah Kew[3], Maja Vahlberg[4], Roop Singh[4], Dorothy Heinrich[4], Julie Arrighi[4,5,6], Maarten van Aalst[4,6,14], Lisa Thalheimer[14], Emmanuel Raju[15], Mathias Hauser[1], Martin Hirschi[1], Lukas Gudmundsson[1], Hiroko K. Beaudoing[7,8], Matthew Rodell[7], Sihan Li[9], Wenchang Yang[10], Gabriel A. Vecchi[10,11], Robert Vautard[12], Luke J Harrington[13] and Sonia I. Seneviratne[1]

[1] Institute for Atmospheric and Climate Science, ETH Zurich, Switzerland
[2] Grantham Institute, Imperial College, London, UK
[3] Royal Netherlands Meteorological Institute (KNMI), De Bilt, The Netherlands
[4] Red Cross Red Crescent Climate Centre, The Hague, Netherlands
[5] Global Disaster Preparedness Center, Washington DC, USA
[6] University of Twente, Enschede, Netherlands
[7] Hydrological Sciences Lab, NASA GSFC, Greenbelt, MD, USA
[8] Earth System Science Interdisciplinary Center, University of Maryland, College Park, MD, USA
[9] Department of Geography, University of Sheffield
[10] Department of Geosciences, Princeton University, Princeton, NJ 08544, USA
[11] High Meadows Environmental Institute, Princeton University, Princeton, NJ 08544, USA
[12] Institut Pierre-Simon Laplace (IPSL), CNRS, Paris, France
[13] Te Aka Mātuatua School of Science, University of Waikato, Hillcrest, Hamilton 3214, New Zealand
[14] International Research Institute for Climate and Society, Columbia University, New York, NY, US
[15] Center for Policy Research on Energy and the Environment, Princeton University, Princeton, USA
[16] Department of Public Health, University of Copenhagen, Denmark

Main findings

- Heat and low rainfall in West-Central Europe had far reaching impacts on a variety of sectors including human health, energy, agriculture, and municipal water supply. It was exacerbated by e.g. poor water infrastructure and leakages, and it came at a time when food and energy prices were already high resulting in compounding social and economic impacts.
- In this study, we particularly focus on the dry soils which caused severe economic and ecological impacts across the Northern Hemisphere (excluding the tropical regions) and were particularly severe in West-Central Europe. We therefore focus on these two regions, North-Hemisphere extratropics and West-Central Europe, to analyse the agricultural and ecological drought from June to August 2022.
- Observation-driven land surface models show that very low summer surface and root-zone soil moisture, such as observed in 2022, happens about once in 20 years in today's climate in both regions.
- While the magnitude of historical trends vary between different observation-based soil moisture products, all agree that the dry conditions observed in 2022 over both regions would have been less likely to occur at the beginning of the 20th century.
- To determine the role of climate change in these observed changes, we combine the observation-based datasets with climate models and conclude that human-induced climate change increased the likelihood of the observed soil moisture drought events. The change in likelihood is larger in the observation-based data compared to the models.
- We also assessed the role of climate change in temperature and rainfall in these regions and found that the strong increase in high temperatures is the main reason for the increased drought.
- Combining all lines of evidence we find for West-Central Europe that human-induced climate change made the 2022 root zone soil moisture drought about 3-4 times more likely, and the surface soil moisture drought about 5-6 times more likely.
- For the Northern Hemisphere extratropics, human-induced climate change made the observed soil moisture drought much more likely, by a factor of at least 20 for the root zone soil moisture and at least 5 for the surface soil moisture, but – as is usually the case with hard to observe quantities – the exact numbers are uncertain.
- The models analysed also show that soil moisture drought will continue to increase with additional global warming, which is consistent with projected long-term trends in climate models as reported e.g., in the IPCC AR6.

1 Introduction

In Europe, above-average air temperatures have been reported from the beginning of 2022, and spring — in the south also winter — was dry over most of the continent (Toreti et al., 2022). In the subsequent 2022 summer, a sequence of heatwaves, combined with widespread precipitation shortages, fostered hot and dry conditions. The European 2022 summer was assessed "hottest on record" by the European Union's environmental programme Copernicus, and was characterised by desiccating soils, particularly in Western regions (Copernicus, 2022), in the wake of the recent heatwaves. Based on runoff anomalies, it was also highlighted in the press in mid-August that the 2022 European drought could be the "worst in 500 years" (The Guardian, 13 Aug 2022). But summer heat and drought were not restricted to Europe; e.g., Mainland China was ravaged by exceptionally high temperatures and aridity (BBC, 17 Sept 2022), and North America experienced an unusually warm summer (Copernicus, 2022). In the midlatitudes, extreme summer heat and precipitation shortages are typically fostered by persistent, often nearly-stationary anticyclones (e.g., Li et al., 2020), or subtropical ridges (e.g., Sousa et al., 2020), and many areas in Europe were subject to the strongest 500 hPa geopotential height anomalies since 1950, between May and July 2022 (Toreti et al., 2022). The strength and meandering of the extratropical jet stream can simultaneously promote hot and dry conditions as well as heavy precipitation in different regions (e.g., Lau & Kim, 2012), yet the understanding of the dynamics underlying such weather extremes and especially their associated future changes remains limited. Nevertheless, to provide an example of the ongoing efforts and resulting discoveries, a recent study has suggested that many heatwaves in the ongoing century in Western Europe have been caused by a double-jet configuration, which is closely linked to anticyclonic flow and has increased in both frequency and persistence (Rousi et al., 2022). From a global perspective, ENSO has remained in the "La Niña" phase since late 2020 (WMO, 2022), which may have contributed to the hot and dry conditions in parts of both China and of North America (Wang et al., 2007, Karori et al., 2013).

While the roles of such and other local and remote dynamic and thermodynamic drivers for the dry and hot summer 2022 are yet to be investigated in detail, it is already clear that the soils in large parts of the Northern Hemisphere extratropics were unusually dry. As such, enhanced land–atmosphere coupling (e.g., Seneviratne et al., 2006, Mueller and Seneviratne 2012, Miralles et al., 2019, Stegehuis et al., 2021) likely contributed to heatwaves in Europe, China, the southwestern United States (NASA Earth Observatory, 2022), and other regions — large parts of the Northern Hemisphere extratropics — experienced a hot and dry summer. On the other hand, the high temperatures were likely a main driver for dry soil conditions due to increased land evapotranspiration, as identified in recent drought events in Europe (e.g. Seneviratne et al. 2012, Teuling et al. 2013) and in a detected trend towards decreased water-availability in the dry season across land regions in the recent past (1985-2014) vs the first half of the 20th century (Padron et al. 2020). Furthermore, the mechanism of northward 'drought propagation' — a causal link between (spring) drought in the Mediterranean, and hot and dry summers in West-Central Europe (Vautard et al., 2005; Zampieri et al., 2009) — may also have played a role in the evolution of the 2022 European drought. The extreme conditions manifested in some of the most severe soil moisture droughts on record; e.g., in July 2022, nearly half of Europe was at warning levels (European Commission, JRC, 2022), with in some areas shortages of drinkable water due to low levels of the water table, whereas China issued its first nationwide drought alert (Reuters, 2022). In addition,

the combination of hot and dry conditions in Europe strongly increased fire risk, leading to the highest burnt area ever recorded since the start of measurements (EFFIS, 2022;).

Low soil moisture typically implies increased water stress for natural vegetation and crops (e.g., Berg & Sheffield, 2018), which can be further exacerbated by elevated air temperatures and hence heat stress (Seneviratne et al. 2021). This is why in Europe, summer crop yields have been "substantially reduced" (Toreti et al., 2022), and food prices in China — especially for fruits and vegetables — were driven up by the heat and drought (NY Times, 26 Aug 2022). Indeed, one of the major impacts of the 2022 drought is crop loss, which poses increasing threats to food security not only in the affected regions, but also globally. While strong evidence for human-induced aggravations of recent heatwaves has been reported repeatedly (Seneviratne et al., 2021), such as for the heatwave in Western Europe in July 2022, there are more uncertainties in the contribution of anthropogenic climate change to trends in agricultural drought conditions in single regions, although the 6th Assessment Report from the Intergovernmental Panel on Climate Change (IPCC) has concluded that there is *medium confidence* that human-induced climate change has contributed to increases in agricultural and ecological droughts in some regions due to evapotranspiration increases (Seneviratne et al., 2021).

In this study, we investigate the role of climate change in the frequency and magnitude of low soil moisture during June-August 2022 for two spatial extents (**Fig. 1**). The first is a large region covering the entire Northern Hemisphere extratropics (NHET) — the land area between 23.5 °N to 90 °N. The second is a smaller region over Europe, demarcated as the West-Central Europe (WCE) region in IPCC AR6 (see Fig. 1b in Iturbide et al., 2020). We report the results for the surface and the root-zone soil moisture that are, respectively, measures of rapid drying and of agricultural droughts that typically evolve over longer periods, with timescales of weeks to months. We focus our analysis on the boreal summer season that spans the June-July-August (JJA) months when the spatial extent of droughts in the Northern Hemisphere is highest (Lu et al., 2019), as has also been the case for the widespread drought of this year (e.g., Toreti et al., 2022; BBC News, 17 Sep 2022). As temperature and precipitation anomalies are known to strongly influence agricultural drought, we also analyse JJA mean temperature and JJA mean precipitation over the same regions as for soil moisture.

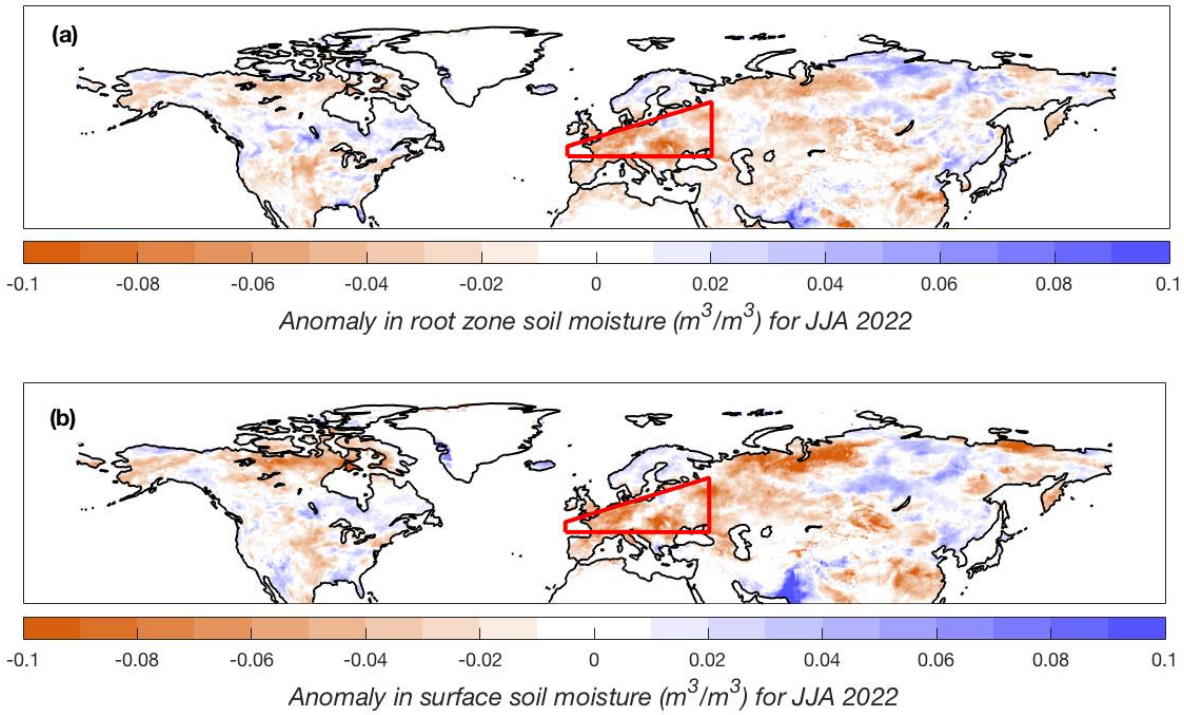

Fig. 1 (a) Anomaly in the JJA average root zone soil moisture w.r.t 1950-2022 climate over the NHET region, plotted using the ERA5-Land dataset. The WCE region is highlighted by the red box. **(b)** *same as (a)* for surface soil moisture.

2 Data and methods

2.1 Observational data

We examine trends in surface and root zone soil moisture over the two selected regions — NHET and WCE as shown in **Fig. 1** — for quantifying the role of climate change in the widespread drought of 2022 that impacted large parts of the Northern Hemisphere. We compare the results for these variables and regions with the respective estimates based on precipitation and temperature to gain insights on how the soil moisture drought has been influenced by the accompanying precipitation deficits and anomalously high temperatures.

The first dataset used in this study, the ERA5 reanalysis product by ECMWF, contains simulated estimates of the climate variables for the period 1950-present, at 31 km resolution and at hourly intervals. We use the data on four variables; precipitation, temperature and volumetric soil moisture at surface (0–7cm) and root zone levels (0–100cm). This product uses the ECMWF assimilation system IFS (IFS Cycle 41R2), and combines historical observations as well as reprocessed datasets as inputs for its land surface model Hydrology Tiled ECMWF Scheme for Surface Exchanges over Land (H-TESSEL).

Due to larger uncertainties in soil moisture estimates from the reanalysis products, on account of it being a derived variable that is affected by the differences in the land surface models and the model setups used, we include estimates from two additional sources for increasing the confidence in our results. The first one is the ERA5-Land product from ECMWF, which is essentially a high resolution

version (9 km) of ERA5 produced only for the land surface, also available from 1950-present. The differences in the estimates from ERA5 and ERA5-Land are attributed to the model formulation and resolution. The land-atmosphere interactions in the IFS for ERA5 are fully coupled, whereas for ERA5-Land, the land surface model H-TESSEL is run offline, forced by ERA5 atmospheric conditions (Muñoz-Sabater et al., 2021; Rosnay et al., 2016). The second source is the NASA Global Land Data Assimilation System Catchment Land Surface Model (GLDAS-CLSM; Rodell et al., 2004). Initialised using the soil moisture and spatial fields from LSM climatology for January 1, 1948, the simulations are forced by the global meteorological forcing data from Princeton University (Sheffield et al., 2006). This model simulates soil moisture data at 0.25° × 0.25° resolution, which is available from 1948-present. From 2003 onwards, Gravity Recovery and Climate Experiment (GRACE) data are assimilated, though we note that at the time of the study, GRACE data had only been available up to and including June 2022. The latter simulation is forced by the operational ECMWF IFS meteorological dataset and assimilates the GRACE/GRACE-FO dataset from University of Texas (Save et al., 2016; Save, 2020) using the Land Information System (Kumar et al., 2016). More details on this dataset are available on the website.

For the WCE region, we additionally analyse E-OBS (version 25.0e). The E-OBS dataset is a 0.25° × 0.25° gridded temperature and precipitation dataset of Europe, formed from the interpolation of station-derived meteorological observations (Cornes et al., 2018). E-OBS was used to produce seasonal cycles and climatology and for trend analysis of precipitation and temperature over Europe.

Finally, as a measure of anthropogenic climate change, we use the (low-pass filtered) global mean surface temperature (GMST), where GMST is taken from the National Aeronautics and Space Administration (NASA) Goddard Institute for Space Science (GISS) surface temperature analysis (GISTEMP, Hansen et al., 2010 and Lenssen et al. 2019). GMST is smoothed with a 4-year running mean.

2.2 Model and experiment descriptions

For this study, we use three multi-model ensembles from climate modelling experiments using very different framings (Philip et al., 2020): Sea Surface temperature (SST) driven global circulation high resolution models and coupled global circulation models.

The first set of models used in this analysis comes from the CMIP6 experiment (Eyring et al., 2016). For all simulations, the period 1850 to 2015 is based on historical coupled simulations, while the SSP5-8.5 scenario is used for the remainder of the 21st century. Models are excluded if they do not provide all relevant variables, do not cover 1850–2100, or include duplicate time steps or missing time steps. The first available ensemble member is used for each model.

The second set of models used in the analysis include the AM2.5C360 (Yang et al. 2021, Chan et al. 2021) and the FLOR (Vecchi et al. 2014) high-resolution climate models developed at Geophysical Fluid Dynamics Laboratory (GFDL). The AM2.5C360 is an atmospheric GCM based on that in the FLOR model (Delworth et al. 2012, Vecchi et al. 2014) with a horizontal resolution of 25 km. Ten ensemble simulations of the Atmospheric Model Intercomparison Project (AMIP) experiment (1871-2021) are analysed. These simulations are initialised from ten different pre-industrial conditions but forced by the same SSTs from HadISST1 (Rayner et al. 2003) after groupwise adjustments (Chan et al. 2021), as well as the same historical radiative forcings. The FLOR model, on the other hand, is an

atmosphere-ocean coupled GCM with a resolution of 50 km for land and atmosphere and 1 degree for ocean and ice. Ten ensemble simulations from FLOR are analysed, which cover the period from 1860 to 2100 and include both the historical and RCP4.5 experiments driven by transient radiative forcings from CMIP5 (Taylor et al. 2012).

The third ensemble considered in this study is the HighResMIP SST-forced model ensemble (Haarsma et al. 2016), the simulations for which span from 1950 to 2050. The SST and sea ice forcings for the period 1950-2014 are obtained from the 0.25° x 0.25° Hadley Centre Global Sea Ice and Sea Surface Temperature dataset that have undergone area-weighted regridding to match the climate model resolution. For the 'future' time period (2015-2050), SST/sea-ice data are derived from RCP8.5 (CMIP5) data, and combined with greenhouse gas forcings from SSP5-8.5 (CMIP6) simulations (see Section 3.3 of Haarsma et al. 2016 for further details). It is worth noting that this ensemble only has outputs for moisture in the upper portion of the soil column (i.e., the upper 10cm of the soil layer), but not moisture in the total soil column, therefore is not considered in the analysis of root zone soil moisture.

2.3 Statistical methods

In this study we analyse JJA series soil moisture, precipitation and temperature values, for both the WCE region and the Northern hemisphere, as defined in Section 1. Methods for observational and model analysis and for model evaluation and synthesis are used according to the World Weather Attribution Protocol, described in Philip et al. (2020), with supporting details found in van Oldenborgh et al. (2021), Ciavarella et al. (2021) and here.

The analysis steps include: (i) trend calculation from observations; (ii) model validation; (iii) multi-method multi-model attribution and (iv) synthesis of the attribution statement.
We calculate the return periods, Probability Ratio (PR; the factor-change in the event's probability) and change in intensity of the event under study in order to compare the climate of now and the climate of the past, defined respectively by the GMST values of now and of the preindustrial past (1850–1900, based on the Global Warming Index https://www.globalwarmingindex.org). To statistically model the event under study, we use a Gaussian distribution that scales (soil moisture, precipitation) or shifts (temperature) with GMST, similar to the analyses in Kew et al. (2021) and Philip et al. (2020). Next, results from observations and models that pass the validation tests are synthesised into a single attribution statement.

3 Observational analysis: return period and trend

3.1. Analysis of atmospheric circulations

Atmospheric circulations in the summer of 2022 were outstanding. The geopotential height, taken from the ERA5 reanalysis, reached record values (Toreti et al., 2022), but also individual daily weather patterns over Western Europe were highly anomalous. In order to measure the departure of regional circulations in 2022 from those of other summers, we carried out a circulation analogue analysis (see, e.g., Yiou et al., 2007). Two atmospheric circulations are considered to be "analogues" when the pattern correlation r of their associated 500 hPa geopotential height exceeds some threshold. Using pattern correlation as a measure of similarity instead of Euclidean distance between fields avoids thermal expansion effects. We use here r=0.7 as a threshold, with a pattern correlation calculated over Western Europe and the Eastern Atlantic [30W-20E;30N-60N], comparisons being made with patterns in the

summer season (JJA). We counted the frequency of analogues of each of the 92 daily circulations of the summer season of 2022 found in other years since 1950. We also counted in a similar way the frequency of analogues of days within other summer seasons from 1950 to 2021 (analogue dates outside the search year), and report the resulting time series in **Fig. 2**. We found that the frequency of analogues of daily circulations in other summers was about 2.5% while the average frequency for other years is about 3.8%.

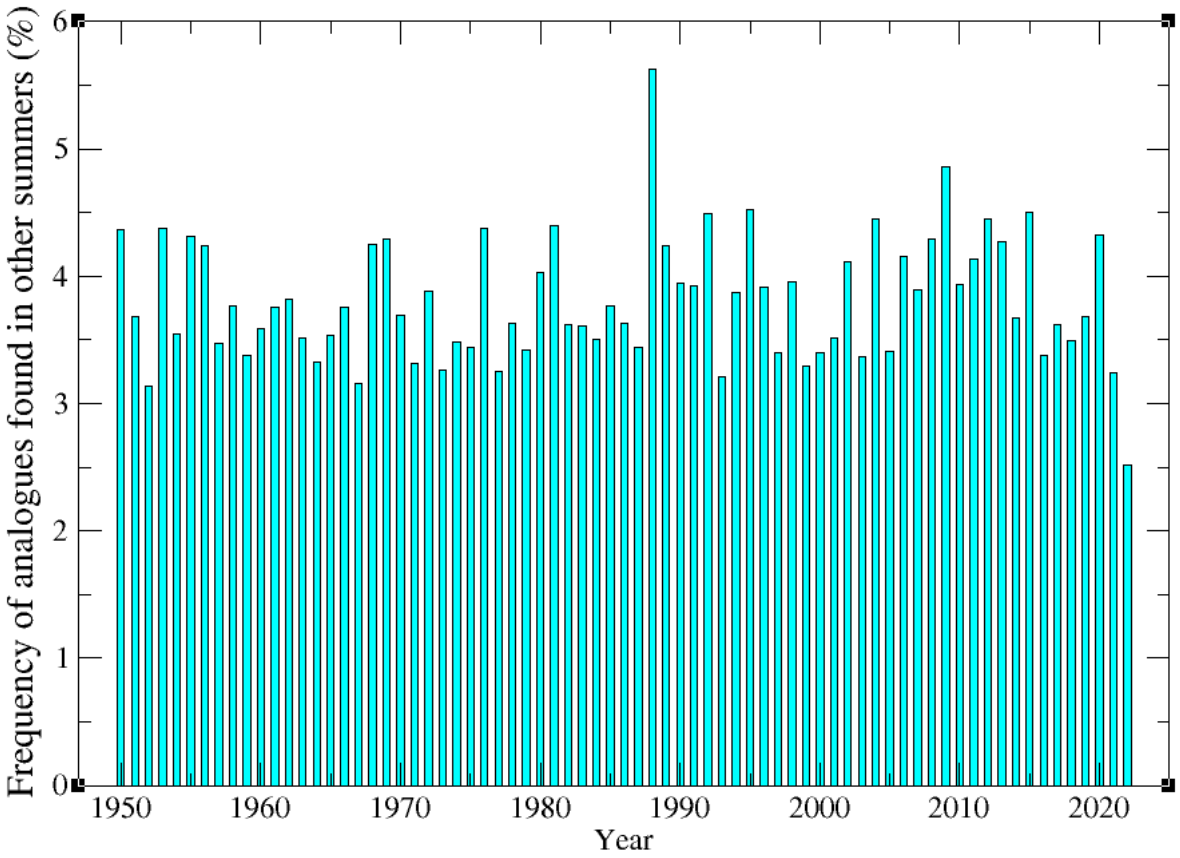

Fig. 2: Average daily frequency of analogues, for each summer season from 1950 to 2022; analogues, characterised by a pattern correlation larger than 0.7, are sought in other summer seasons.

Such an analysis was carried out for the exceptional summer short heat waves of 2019 (Vautard et al., 2019, 2020), but the heatwave periods were short and significant trends in analogues could not be identified either.

Hot periods (around days 15-20, 45-55 in particular, are associated with anomalously rare circulations, some days having no analogue with pattern correlation larger than 0.7 in previous years. These hot periods are generally associated with a persisting cut-off low off the coasts of Portugal, allowing a southerly flow to bring hot and dry air from Spain and Sahara. This type of anomalous circulation condition is illustrated in the geopotential height field map of the 18 June 2022 00 UTC (**Fig. 3**); 18 June had an extremely low frequency of past analogs (0.14%). In general, such circulations with a low pressure system over the North-East Atlantic, coupled with an anticyclone over Europe, were shown to favour extreme temperatures in the case of dry soils (Quesada et al., 2012) and therefore further intensify drought.

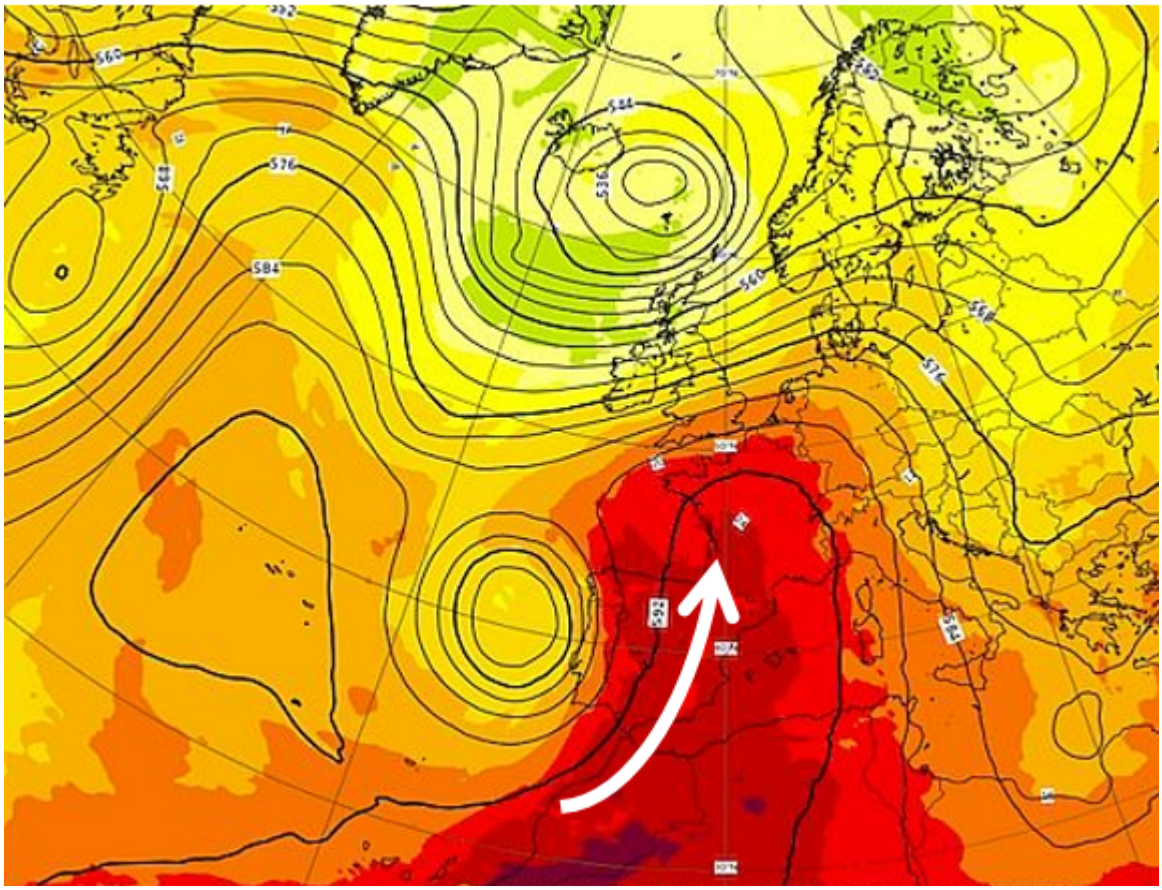

Fig. 3: ECMWF analysis of the 18 June 2022 00 UTC of the 500 hPa geopotential height (isolines) with superimposed temperature at 850 hPa. The arrow shows the direction of the large-scale flow, transporting heat of Saharan origin into Western Europe.

3.2 Analysis of gridded data

3.2.1 WCE region

Fig. 4 shows the trend fitting methods described in Philip et al. (2020) applied to the 1950–2022 JJA average surface soil moisture and averaged over the WCE region, based on 3 datasets — ERA5-Land (**Fig. 4(a)**), ERA5 (**Fig. 4(b)**) and GLDAS-CLSM (**Fig. 4(c)**). The left panels show the variable as a function of the GMST anomaly, while the right panels show the Gaussian distribution-based return period curves for this variable in the present 2022 climate (red lines) and the past climate when the global mean temperature was 1.2°C cooler (blue lines) for each of these datasets. Similar plots for the JJA average root zone soil moisture, averaged over the WCE region, are shown in **Fig. 5**. The return period of the surface soil moisture in the 2022 climate are 13, 14 and 17 years, from the ERA5-Land (**Fig. 4**(a *right*)), ERA5 (**Fig. 4**(b *right*)) and GLDAS-CLSM (**Fig. 4**(c *right*)) datasets, respectively. The return periods of the 2022 observed root zone soil moisture are also found to be consistent across the different datasets in terms of the order of magnitude, ranging from 12 to 30 years (right panels in **Fig. 5**). Therefore, we round this to 20 years for both variables for the remainder of the analysis.

Analysing the three observational datasets individually, they each show significant changes towards drought conditions for surface soil moisture between the past and present climates (**Fig. 4**; **Table 4**), with probability ratios of at least 7, for ERA5, at least 3 for ERA5-Land, and higher orders of magnitude for GLDAS-CLSM. Soil moisture decreased during this period by around 10% for ERA5, 8% for ERA-

Land and 14% for GLDAS-CLSM. For the root-zone, ERA5-Land gave similar results to the surface layer, with a PR of at least 4 and a decrease in soil moisture of 9%, while ERA5 and GLDAS-CLSM gave stronger signals with PRs in excess of 200 and decreases in soil moisture exceeding 14% (**Fig. 5**; **Table 5**).

We also repeat this analysis for the JJA average temperature and precipitation for the WCE region (Appendix Figs. A1 & A2). Temperature shows very strong trends with probability ratios of at least 170 for E-OBS data and even much larger for ERA5 data. This corresponds to a change in intensity of about 1.7 to 2 degrees (for details see Appendix Table A1). The return period used for the model analysis of temperature in the WCE region is 20 years. Trends in precipitation are much smaller and encompass no change, see Appendix Table A2 for details. The return period used for the model analysis of a low precipitation event in the WCE region is 10 years.

We note that to facilitate comparisons between different models and the observation-driven products, all soil moisture data were scaled prior to analysis by dividing through the respective 1950–2022 JJA standard deviation. Moreover, ERA5, ERA5-Land and GLDAS-CLSM soil moisture data were separately analysed for a reduced time period of 1980–2022 (not shown), since the data prior to 1980 are considered to be less reliable — largely due to a lack of satellite data. To enable a comparison, and contrary to the approach selected for the actual analysis, the data were scaled using 1980–2022 as a reference for the standard deviation for 1950–2022 and 1980–2022. For all observation-based datasets, return periods of both surface and root-zone soil moisture are generally lower when analysing only 1980 onwards, yet still comparable (e.g., 10 instead of 20 years). Probability ratios tend to be higher for the reduced time period (1980–2022), but are deemed unreliable due to the short records. Since the remaining statistical parameters do not strongly depend on the time period, we proceed with as much data as possible and hence 1950–2022.

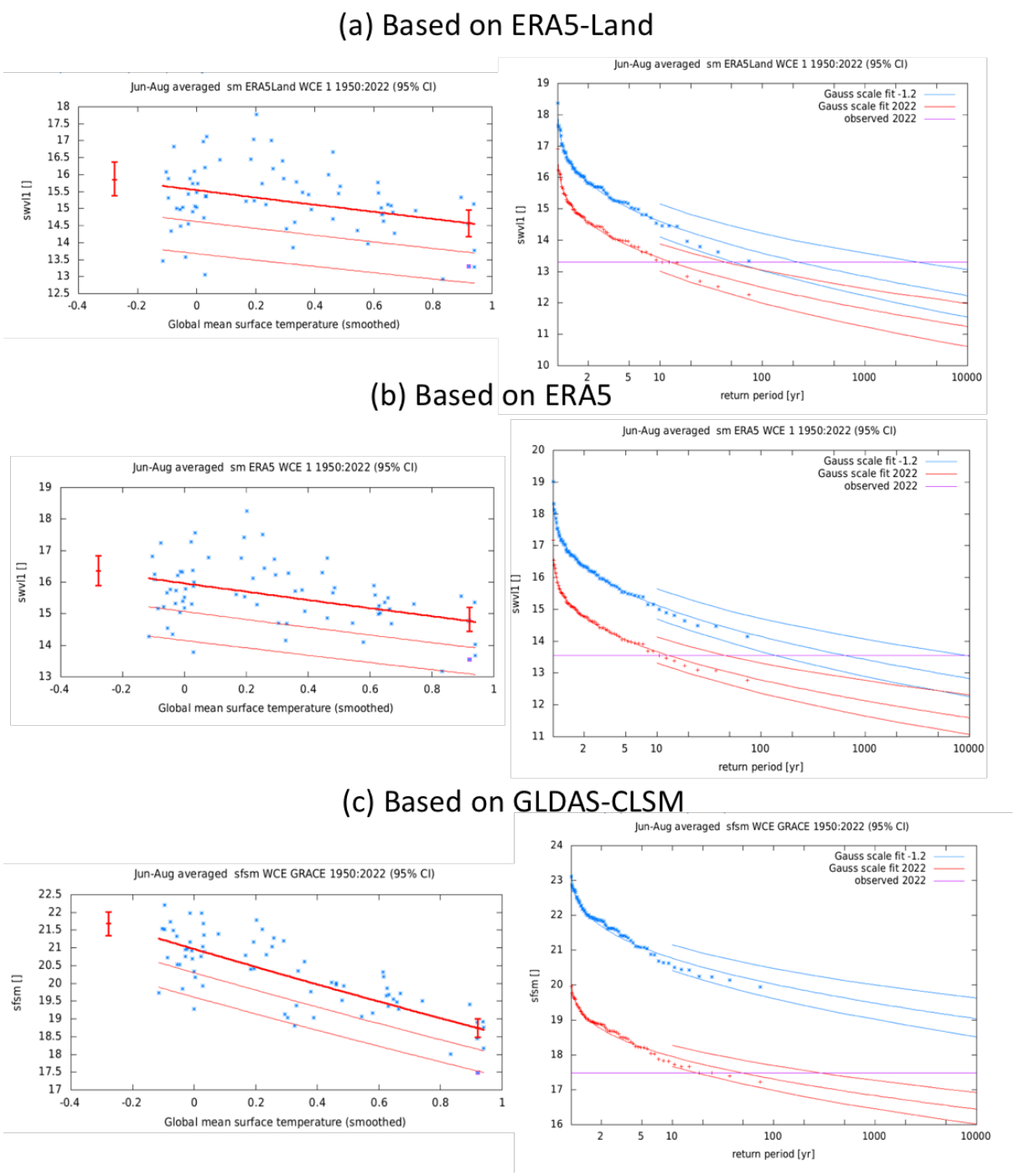

Fig. 4: Surface soil moisture. Gaussian fit with constant dispersion parameter, and the location parameter scaling proportional to GMST of the index series, for the WCE region based on three gridded datasets- (a) ERA5-Land (b) ERA5 and (c) GLDAS-CLSM. The 2022 event is included in the fit. **Left**: Observed JJA average surface soil moisture as a function of the smoothed GMST. The thick red line denotes the time-varying location parameter. The vertical red lines show the 95% confidence interval for the location parameter, for the current, 2022 climate and a 1.2ºC cooler climate. The 2022 observation is highlighted with the magenta box. **Right**: Return time plots for the climate of 2022 (red) and a climate with GMST 1.2 ºC cooler (blue). The past observations are shown twice: once shifted up to the current climate and once shifted down to the climate of the late nineteenth century. The markers show the data and the lines show the fits and uncertainty from the bootstrap. The magenta line shows the magnitude of the 2022 event analysed here.

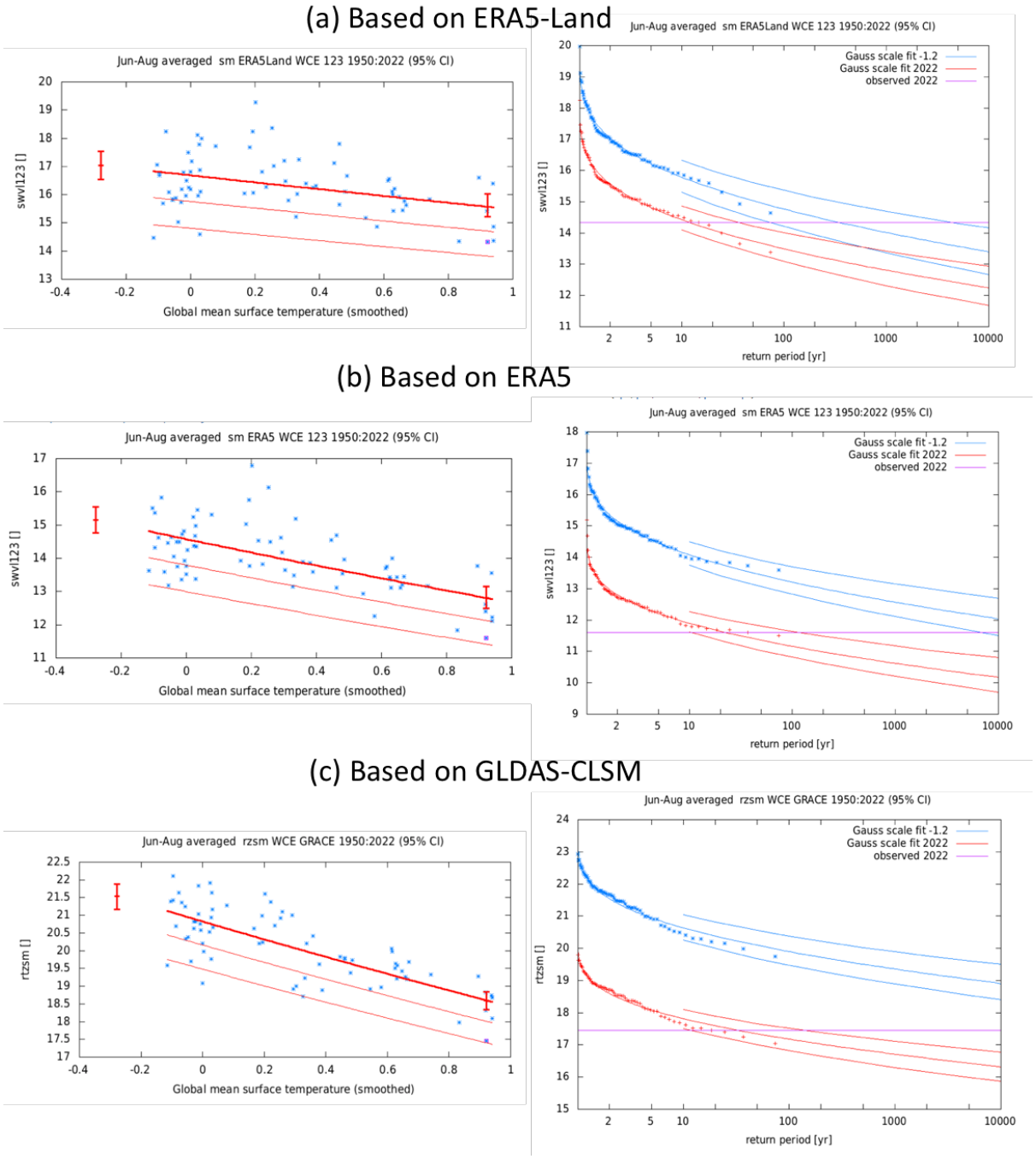

Fig. 5: *same as* Fig. 4, for **root zone soil moisture**.

3.2.2 NHET region

For the NHET region, the gridded data sets ERA5, ERA5-Land and GLDAS-CLSM are used to represent observed surface and ERA5-Land and GLDAS-CLSM are used to represent root-zone soil moisture. **Fig. 6** shows the trend fitting results based on these datasets, for JJA average surface soil moisture. The return periods for the 2022 event are found to be consistent across the datasets, ranging from 16 to 20 years. The changes are clearly towards more frequent drought, with ERA5 and ERA5-Land giving a probability ratio of around 170 (18 - 6000), and GLDAS-CLSM a much larger ratio. The corresponding changes in intensity show that surface soil moisture has decreased by around 2.7% (1.4%

to 3.8%) for ERA5, 2.6% (1.5% to 3.6%) according to ERA5-Land, and has decreased by around 4.4% (3.7% to 5%) according to GLDAS-CLSM (**Table 7**). The estimates from the ERA-based products and the GLDAS do not overlap in their confidence intervals, indicating that the magnitude of the observed trend is difficult to quantify and is sensitive to the dataset used, however both datasets indicate a clear tendency towards drought conditions. In the synthesis, the uncertainty related to the large difference between their estimates is included for each of these datasets in addition to the standard sampling uncertainty.

For root zone soil moisture, the return period ranges from 10 to 20 years (**Fig. 7**). However, for ERA5, we note that response of the root zone soil moisture to the GMST is possibly suppressed (see *left panel* in **Fig. 7**(b)), as compared to the other datasets (**Fig. 7**(a) and **Fig. 7**(c)). A quick examination of the data revealed inconsistencies in the data around Greenland for this variable that warrants a detailed examination. Therefore, in this rapid study, we exclude the ERA5-based results from subsequent analysis of root zone soil moisture in the NHET region. The ERA5-Land-based data gives a probability ratio of around 650 (40 to 50,000) and GLDAS-GLSM even larger. The corresponding changes in intensity of root-zone soil moisture are a 2.4% decrease (3.2% decrease to 1.4% increase) for ERA5-Land, and a 3.1% decrease (3.6% decrease to 2.7%decrease) for GLDAS-GLSM. In this case, there is an overlap in the confidence intervals of the two datasets on the side of change towards drought conditions.

We also repeat this analysis for the JJA average temperature and precipitation for the NHET region (Appendix Figs. A3 & A3). Temperature shows very strong trends with very high Probability ratios for ERA5 data, indicating that such a hot summer would have been virtually impossible without climate change. The corresponding change in intensity is about 1.9°C (95% CI 1.7°C to 2.1°C) (for details see Appendix Table A3). The return period used for the model analysis of temperature in the NHET region is 10 years. As for the WCE region the trend in precipitation is much smaller and encompasses no change, see Appendix Table A4 for details. The return period used for the model analysis of a low precipitation event in the NHET region is 10 years.

(a) Based on ERA5-Land

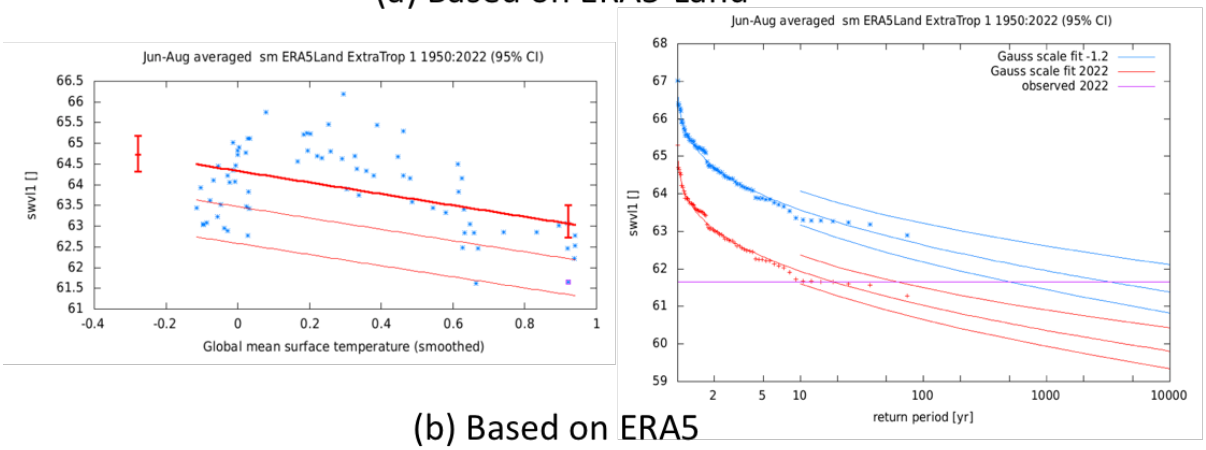

(b) Based on ERA5

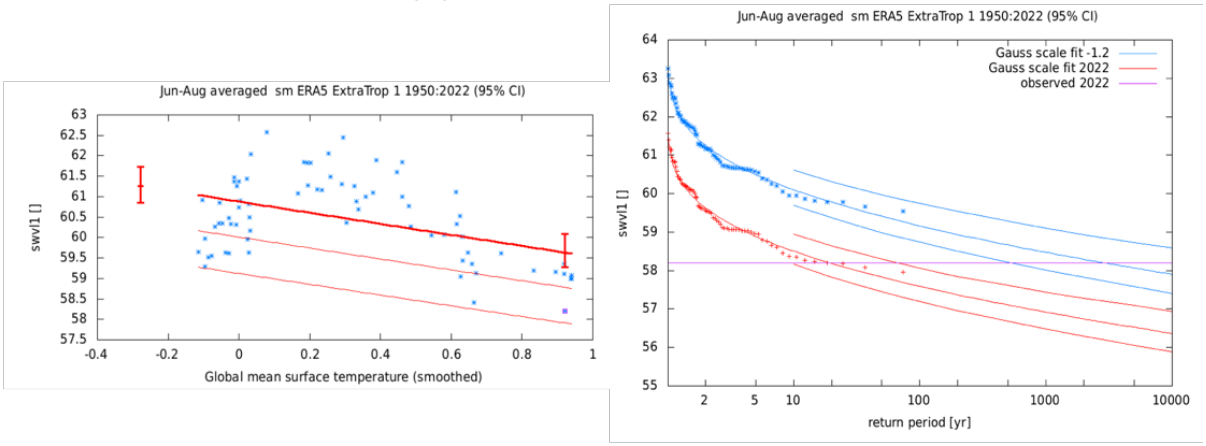

(c) Based on GLDAS-CLSM

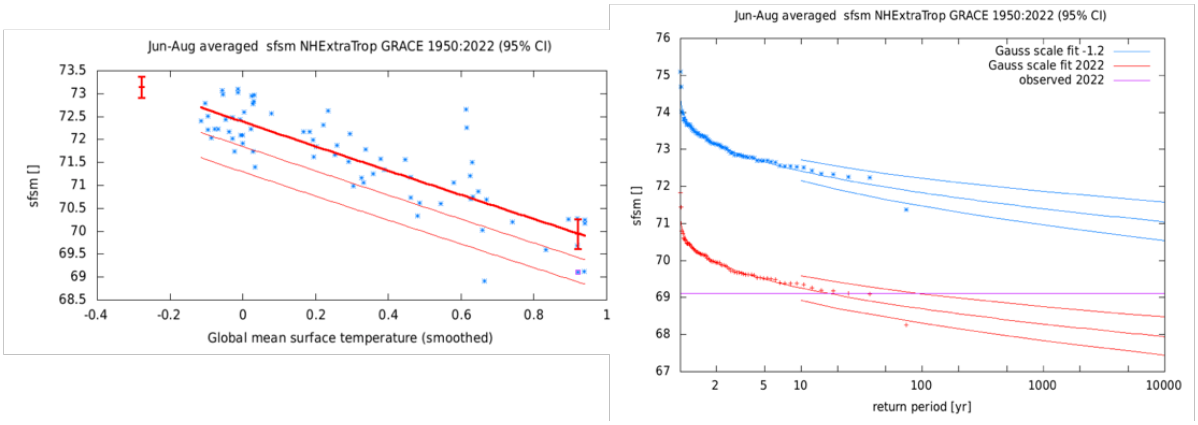

Fig. 6. *same as* Fig. 4, for **JJA average surface soil moisture over the NHET region**.

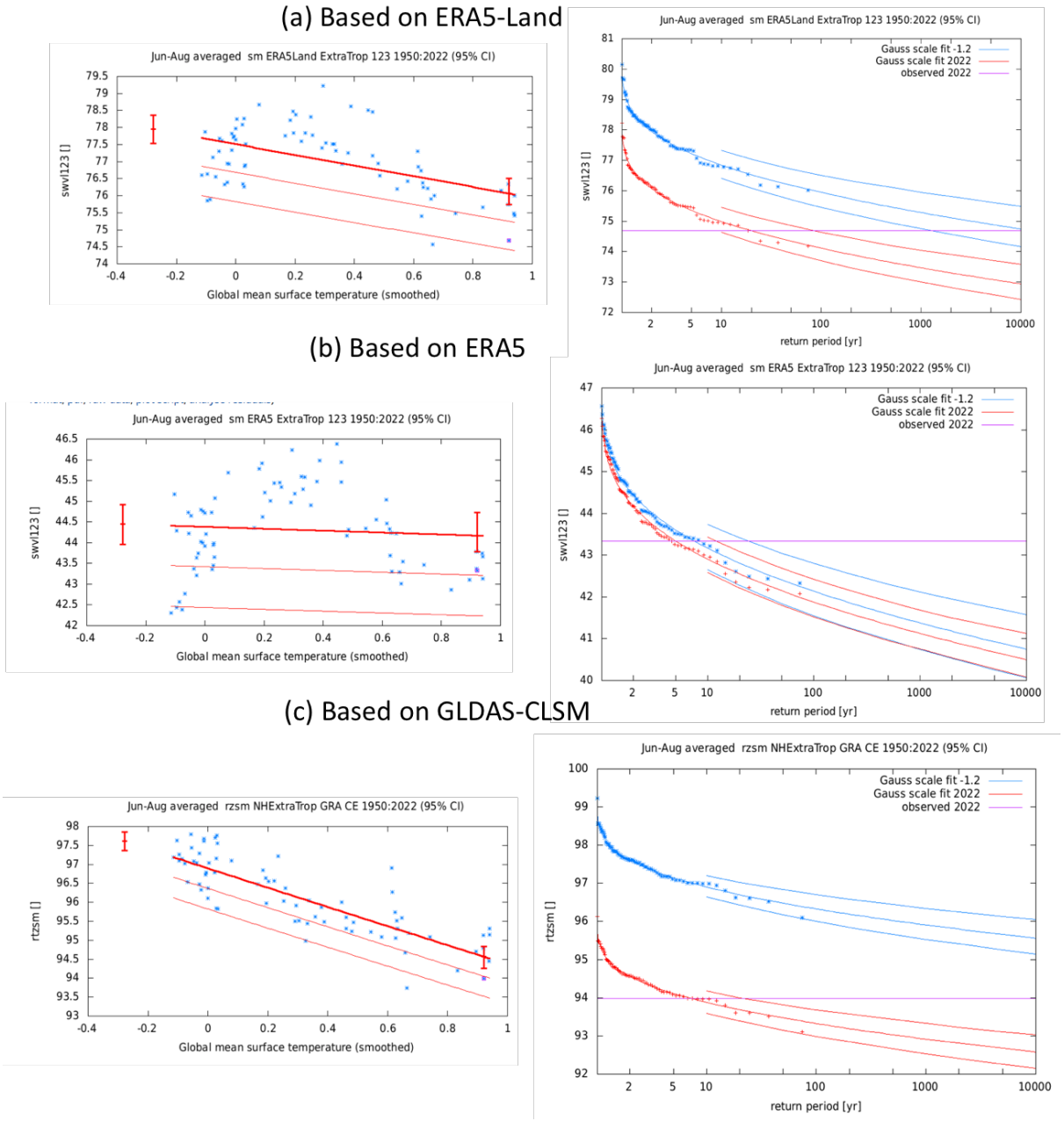

Fig. 7. *same as* Fig. 4, for **JJA average root zone soil moisture over the NHET region**.

4 Model evaluation

For this study, and bearing in mind the large uncertainty of observation-driven soil moisture products due to the different land surface models employed and their inherent deficiencies (Gevaert et al., 2018), as well as the limitations of remote sensing particularly for the root-zone soil moisture (Babaeian et al., 2019), we rely on precipitation and temperature as proxies for moisture supply and demand. Rather than directly evaluating the statistical parameters for soil moisture, we require all models to pass validation for the respective domain (WCE, NHET) for both precipitation and temperature. For these variables, we assess the models' fitness for purpose in three ways. Firstly, we qualitatively compare the seasonal cycles in models to observations, checking for the timing and relative amplitudes of peaks and troughs; secondly, we compare the spatial pattern of maximum temperatures averaged over June–August for Europe (WCE) and the entire Northern Hemisphere extratropics (NHET), respectively. Thirdly, we

check if the parameters of the fitted statistical distribution (Gaussian shifting with GMST for temperature, Gaussian scaling with GMST for precipitation) in models are compatible with those from observations, as shown below. For the observational parameter range, wherever applicable, all of the respective listed observation-based datasets are considered. Models whose statistical parameter range lies within the observational range (95% confidence interval) are considered as 'good', whereas overlapping ranges are 'reasonable'. Additionally, wherever available, the seasonal cycle and spatial pattern of soil moisture were also evaluated against ERA5-land estimates- these were typically found to be 'reasonable' in those models that passed the combined P & T validation. **Tables 1 & 2** show the model evaluation results for the surface and root zone soil moisture, respectively, for the WCE region. **Tables 3 & 4** show these results for the NHET region. Only models with an overall performance of 'reasonable' or better were used for the attribution analysis. Based on the capability of the model to capture the seasonal cycle, spatial pattern and statistical properties for temperature and precipitation, a model must pass 6 checks (or 8 if soil moisture seasonal cycle and spatial pattern available for evaluation) — without a single 'bad' performance.

Table 1. Evaluation results for the climate models considered for the attribution analysis of JJA **surface soil moisture for WCE region**. The table contains qualitative assessments of seasonal cycle and spatial pattern of precipitation and temperature from the models (good, reasonable, bad) along with estimates for dispersion parameter, shape parameter and event magnitude. The corresponding estimates for observations are shown in blue. The seasonal cycles and spatial patterns for soil moisture are also evaluated, whenever available. Based on overall suitability, the models are classified as good, reasonable and bad, shown by green, yellow and red highlights, respectively.

	Temperature			Precipitation			Surface soil moisture	
Observations			Sigma			Sigma		
E-OBS			0.656 (0.557 ... 0.746)			0.121 (0.101 ... 0.138)		
ERA5			0.654 (0.549 ... 0.739)			0.125 (0.102 ... 0.144)		
Models	Seasonal cycle	Spatial pattern	Sigma	Seasonal cycle	Spatial pattern	Sigma	Seasonal cycle	Spatial pattern
AM2.5C360 amip1871-2021 (10)	reasonable	good	0.838 (0.792 ... 0.880)	reasonable	good	0.142 (0.135 ... 0.149)	<not evaluated>	<not evaluated>
FLOR historical-rcp4.5 (10)	reasonable	good	0.901 (0.851 ... 0.946)	reasonable	good	0.140 (0.132 ... 0.147)	<not evaluated>	<not evaluated>
ACCESS-CM2 historical-ssp585 (1)	reasonable	good	0.917 (0.779 ... 1.09)	reasonable	good	0.131 (0.112 ... 0.154)	reasonable	reasonable

ACCESS-ESM1-5 historical-ssp585 (1)	reasonable	good	0.963 (0.823 ... 1.14)	reasonable	good	0.164 (0.141 ... 0.196)	reasonable	bad
BCC-CSM2-MR historical-ssp585 (1)	reasonable	good	1.19 (1.02 ... 1.43)	reasonable	reasonable	0.181 (0.153 ... 0.215)	reasonable	reasonable
CMCC-CM2-SR5 historical-ssp585 (1)	reasonable	reasonable	1.09 (0.934 ... 1.31)	reasonable	reasonable	0.174 (0.147 ... 0.207)	reasonable	reasonable
CMCC-ESM2 historical-ssp585 (1)	reasonable	good	1.12 (0.951 ... 1.34)	reasonable	reasonable	0.188 (0.162 ... 0.227)	reasonable	reasonable
CanESM5 historical-ssp585 (1)	reasonable	good	0.751 (0.642 ... 0.893)	good	good	0.135 (0.116 ... 0.163)	reasonable	reasonable
EC-Earth3 historical-ssp585 (1)	reasonable	good	0.930 (0.795 ... 1.10)	reasonable	good	0.133 (0.113 ... 0.159)	reasonable	good
GFDL-CM4 historical-ssp585 (1)	good	good	0.746 (0.640 ... 0.887)	good	good	0.101 (0.0870 ... 0.120)	reasonable	reasonable
HadGEM3-GC31-LL historical-ssp585 (1)	reasonable	good	0.756 (0.640 ... 0.898)	reasonable	good	0.138 (0.118 ... 0.167)	reasonable	good
HadGEM3-GC31-MM historical-ssp585 (1)	reasonable	good	0.813 (0.695 ... 0.978)	reasonable	good	0.146 (0.125 ... 0.174)	reasonable	good
IITM-ESM historical-ssp585 (1)	good	reasonable	0.870 (0.749 ... 1.03)	reasonable	good	0.138 (0.117 ... 0.164)	reasonable	bad
INM-CM4-8 historical-ssp585 (1)	reasonable	bad	0.799 (0.684 ... 0.953)	bad	reasonable	0.228 (0.194 ... 0.277)	reasonable	bad

INM-CM5-0 historical-ssp585 (1)	good	reasonable	0.895 (0.768 ... 1.07)	bad	reasonable	0.209 (0.178 ... 0.251)	reasonable	bad
IPSL-CM6A-LR historical-ssp585 (1)	good	good	0.706 (0.602 ... 0.842)	reasonable	good	0.126 (0.108 ... 0.150)	reasonable	bad (very patchy)
KACE-1-0-G historical-ssp585 (1)	reasonable	bad	1.06 (0.906 ... 1.27)	bad	bad	0.264 (0.223 ... 0.319)	bad	bad
MIROC6 historical-ssp585 (1)	reasonable	bad	0.681 (0.578 ... 0.818)	reasonable	reasonable	0.119 (0.101 ... 0.141)	reasonable	reasonable
MIROC-ES2L historical-ssp585 (1)	reasonable	bad	0.634 (0.542 ... 0.759)	reasonable	bad	0.104 (0.0890 ... 0.124)	reasonable	reasonable
MPI-ESM1-2-HR historical-ssp585 (1)	good	good	0.746 (0.637 ... 0.895)	reasonable	good	0.161 (0.138 ... 0.195)	reasonable	good
MPI-ESM1-2-LR historical-ssp585 (1)	good	good	0.756 (0.646 ... 0.898)	reasonable	good	0.133 (0.113 ... 0.158)	reasonable	good
NorESM2-LM historical-ssp585 (1)	reasonable	good	0.838 (0.721 ... 0.997)	reasonable	reasonable	0.183 (0.155 ... 0.222)	reasonable	bad
TaiESM1 historical-ssp585 (1)	reasonable	good	0.969 (0.829 ... 1.16)	reasonable	reasonable	0.180 (0.155 ... 0.214)	reasonable	reasonable
UKESM1-0-LL historical-ssp585 (1)	good	good	0.916 (0.779 ... 1.09)	reasonable	good	0.149 (0.127 ... 0.180)	reasonable	reasonable
EC-EARTH3P (1)	good	good	0.771 (0.644 ... 0.863)	reasonable	good	0.0710 (0.0590 ... 0.0790)	reasonable	<not evaluated>

EC-EARTH3P-HR (1)	good	good	0.659 (0.560 ... 0.748)	good	good	0.128 (0.0180 ... 0.144)	reasonable	<not evaluated>
HadGEM3-GC31-HM (1)	good	good	0.734 (0.616 ... 0.826)	good	good	0.149 (0.123 ... 0.171)	good	<not evaluated>
HadGEM3-GC31-MM (1)	good	good	0.712 (0.614 ... 0.786)	good	good	0.131 (0.110 ... 0.147)	good	<not evaluated>
CNRM-CM6-1-HR (1)	good	good	0.769 (0.650 ... 0.873)	good	good	0.185 (0.153 ... 0.212)	good	<not evaluated>

Table 2. Evaluation results for the climate models considered for the attribution analysis of JJA **root zone soil moisture for WCE region**. The table contains qualitative assessments of seasonal cycle and spatial pattern of precipitation and temperature from the models (good, reasonable, bad) along with estimates for dispersion parameter, shape parameter and event magnitude. The corresponding estimates for observations are shown in blue. The seasonal cycles and spatial patterns for soil moisture are also evaluated, whenever available. Based on overall suitability, the models are classified as good, reasonable and bad, shown by green, yellow and red highlights, respectively.

	Temperature			Precipitation			Root zone soil moisture	
Observations			Sigma			Sigma		
E-OBS			0.656 (0.557 ... 0.746)			0.121 (0.101 ... 0.138)		
ERA5			0.654 (0.549 ... 0.739)			0.125 (0.102 ... 0.144)		
Models	Seasonal cycle	Spatial pattern	Sigma	Seasonal cycle	Spatial pattern	Sigma	Seasonal cycle	Spatial pattern
AM2.5C360 amip1871-2021 (10)	reasonable	good	0.838 (0.792 ... 0.880)	reasonable	good	0.142 (0.135 ... 0.149)	<not evaluated>	<not evaluated>
FLOR historical-rcp4.5 (10)	reasonable	good	0.901 (0.851 ... 0.946)	reasonable	good	0.140 (0.132 ... 0.147)	<not evaluated>	<not evaluated>
ACCESS-CM2 historical-ssp585 (1)	reasonable	good	0.917 (0.779 ... 1.09)	reasonable	good	0.131 (0.112 ... 0.154)	reasonable	reasonable
ACCESS-ESM1-5 historical-ssp585 (1)	reasonable	good	0.963 (0.823 ... 1.14)	reasonable	good	0.164 (0.141 ... 0.196)	reasonable	reasonable
BCC-CSM2-MR historical-ssp585 (1)	reasonable	good	1.19 (1.02 ... 1.43)	reasonable	reasonable	0.181 (0.153 ... 0.215)	good	reasonable
CESM2-WACCM historical-ssp585 (1)	reasonable	good	0.858 (0.738 ... 1.03)	reasonable	reasonable	0.147 (0.125 ... 0.178)	good	reasonable

CESM2 historical-ssp585 (1)	reasonable	good	0.955 (0.816 ... 1.13)	reasonable	reasonable	0.162 (0.138 ... 0.194)	good	reasonable
CMCC-CM2-SR5 historical-ssp585 (1)	reasonable	reasonable	1.09 (0.934 ... 1.31)	reasonable	reasonable	0.174 (0.147 ... 0.207)	reasonable	reasonable
CMCC-ESM2 historical-ssp585 (1)	reasonable	good	1.12 (0.951 ... 1.34)	reasonable	reasonable	0.188 (0.162 ... 0.227)	reasonable	reasonable
CNRM-CM6-1 historical-ssp585 (1)	good	good	0.803 (0.686 ... 0.956)	reasonable	reasonable	0.178 (0.150 ... 0.214)	reasonable	reasonable
CNRM-ESM2-1 historical-ssp585 (1)	good	good	0.835 (0.711 ... 1.00)	reasonable	reasonable	0.190 (0.162 ... 0.228)	reasonable	reasonable
CanESM5 historical-ssp585 (1)	reasonable	good	0.751 (0.642 ... 0.893)	good	good	0.135 (0.116 ... 0.163)	reasonable	reasonable
EC-Earth3-CC historical-ssp585 (1)	good	good	0.865 (0.738 ... 1.03)	reasonable	good	0.145 (0.122 ... 0.175)	good	good
EC-Earth3-Veg-LR historical-ssp585 (1)	good	good	0.778 (0.661 ... 0.928)	reasonable	good	0.123 (0.107 ... 0.147)	reasonable	good
EC-Earth3-Veg historical-ssp585 (1)	good	good	0.874 (0.748 ... 1.04)	reasonable	good	0.154 (0.133 ... 0.187)	reasonable	good
EC-Earth3 historical-ssp585 (1)	reasonable	good	0.930 (0.795 ... 1.10)	reasonable	good	0.133 (0.113 ... 0.159)	reasonable	good
GFDL-CM4 historical-ssp585 (1)	good	good	0.746 (0.640 ... 0.887)	good	good	0.101 (0.0870 ... 0.120)	reasonable	bad

HadGEM3-GC31-LL historical-ssp585 (1)	reasonable	good	0.756 (0.640 ... 0.898)	reasonable	good	0.138 (0.118 ... 0.167)	reasonable	good
KACE-1-0-G historical-ssp585 (1)	reasonable	bad	1.06 (0.906 ... 1.27)	bad	bad	0.264 (0.223 ... 0.319)	bad	bad
MIROC6 historical-ssp585 (1)	reasonable	bad	0.681 (0.578 ... 0.818)	reasonable	reasonable	0.119 (0.101 ... 0.141)	reasonable	reasonable
MPI-ESM1-2-HR historical-ssp585 (1)	good	good	0.746 (0.637 ... 0.895)	reasonable	good	0.161 (0.138 ... 0.195)	good	good
MPI-ESM1-2-LR historical-ssp585 (1)	good	good	0.756 (0.646 ... 0.898)	reasonable	good	0.133 (0.113 ... 0.158)	good	good
MRI-ESM2-0 historical-ssp585 (1)	good	good	0.634 (0.540 ... 0.747)	good	good	0.106 (0.0900 ... 0.126)	reasonable	bad
NorESM2-LM historical-ssp585 (1)	reasonable	good	0.838 (0.721 ... 0.997)	reasonable	reasonable	0.183 (0.155 ... 0.222)	good	reasonable
NorESM2-MM historical-ssp585 (1)	reasonable	good	1.05 (0.900 ... 1.25)	reasonable	reasonable	0.165 (0.138 ... 0.197)	reasonable	reasonable
TaiESM1 historical-ssp585 (1)	reasonable	good	0.969 (0.829 ... 1.16)	reasonable	reasonable	0.180 (0.155 ... 0.214)	bad	reasonable
UKESM1-0-LL historical-ssp585 (1)	good	good	0.916 (0.779 ... 1.09)	reasonable	good	0.149 (0.127 ... 0.180)	reasonable	reasonable

Table 3. Evaluation results for the climate models considered for the attribution analysis of JJA **surface soil moisture for NHET region**. The table contains qualitative assessments of seasonal cycle and spatial pattern of precipitation and temperature from the models (good, reasonable, bad) along with estimates for dispersion parameter, shape parameter and event magnitude. The corresponding estimates for observations are shown in blue. The seasonal cycles and spatial patterns for soil moisture are also evaluated, whenever available. Based on overall suitability, the models are classified as good, reasonable and bad, shown by green, yellow and red highlights, respectively.

	Temperature			Precipitation			Root zone soil moisture	
Observations			Sigma			Sigma		
E-OBS			0.656 (0.557 ... 0.746)			0.121 (0.101 ... 0.138)		

ERA5			0.654 (0.549 ... 0.739)			0.125 (0.102 ... 0.144)		
Models	Seasonal cycle	Spatial pattern	Sigma	Seasonal cycle	Spatial pattern	Sigma	Seasonal cycle	Spatial pattern
AM2.5C360 amip1871-2021 (10)	reasonable	good	0.838 (0.792 ... 0.880)	good	good	0.0290 (0.0280 ... 0.0310)	<not evaluated>	<not evaluated>
FLOR historical-rcp45 (10)	reasonable	good	0.901 (0.851 ... 0.946)	good	good	0.0240 (0.0230 ... 0.0250)	<not evaluated>	<not evaluated>
ACCESS-CM2 historical-ssp585 (1)	reasonable	good	0.917 (0.779 ... 1.09)	good	good	0.0340 (0.0290 ... 0.0410)	reasonable	good
ACCESS-ESM1-5 historical-ssp585 (1)	reasonable	good	0.963 (0.823 ... 1.14)	good	reasonable	0.0240 (0.0210 ... 0.0290)	reasonable	reasonable
BCC-CSM2-MR historical-ssp585 (1)	reasonable	good	1.19 (1.02 ... 1.43)	good	reasonable	0.0290 (0.0240 ... 0.0340)	good	reasonable
CMCC-CM2-SR5 historical-ssp585 (1)	reasonable	reasonable	1.09 (0.934 ... 1.31)	good	good	0.0250 (0.0210 ... 0.0290)	reasonable	reasonable
CMCC-ESM2 historical-ssp585 (1)	reasonable	good	1.12 (0.951 ... 1.34)	good	good	0.0280 (0.0240 ... 0.0330)	reasonable	reasonable
CanESM5 historical-ssp585 (1)	reasonable	good	0.751 (0.642 ... 0.893)	good	good	0.0290 (0.0250 ... 0.0340)	good	reasonable

EC-Earth3 historical-ssp585 (1)	reasonable	good	0.930 (0.795 ... 1.10)	good	good	0.0210 (0.0180 ... 0.0260)	reasonable	good
GFDL-CM4 historical-ssp585 (1)	good	good	0.746 (0.640 ... 0.887)	good	good	0.0280 (0.0240 ... 0.0330)	reasonable	reasonable
HadGEM3-GC31-LL historical-ssp585 (1)	reasonable	good	0.756 (0.640 ... 0.898)	good	good	0.0280 (0.0240 ... 0.0330)	reasonable	good
HadGEM3-GC31-MM historical-ssp585 (1)	reasonable	good	0.813 (0.695 ... 0.978)	good	good	0.0280 (0.0240 ... 0.0330)	reasonable	good
INM-CM4-8 historical-ssp585 (1)	reasonable	bad	0.799 (0.684 ... 0.953)	reasonable	good	0.0210 (0.0180 ... 0.0250)	reasonable	reasonable
INM-CM5-0 historical-ssp585 (1)	good	reasonable	0.895 (0.768 ... 1.07)	reasonable	good	0.0230 (0.0200 ... 0.0270)	reasonable	reasonable
IPSL-CM6A-LR historical-ssp585 (1)	good	good	0.706 (0.602 ... 0.842)	good	good	0.0190 (0.0160 ... 0.0230)	reasonable	bad
KACE-1-0-G historical-ssp585 (1)	reasonable	bad	1.06 (0.906 ... 1.27)	bad	reasonable	0.0380 (0.0320 ... 0.0440)	reasonable	bad
MIROC6 historical-ssp585 (1)	reasonable	bad	0.681 (0.578 ... 0.818)	good	good	0.0220 (0.0190 ... 0.0260)	reasonable	reasonable
MIROC-ES2L historical-ssp585 (1)	reasonable	bad	0.634 (0.542 ... 0.759)	good	reasonable	0.0200 (0.0170 ... 0.0240)	reasonable	reasonable
MPI-ESM1-2-HR historical-ssp585 (1)	good	good	0.746 (0.637 ... 0.895)	good	good	0.0280 (0.0230 ... 0.0320)	reasonable	good

MPI-ESM1-2-LR historical-ssp585 (1)	good	good	0.756 (0.646 ... 0.898)	reasonable	good	0.0230 (0.0200 ... 0.0280)	reasonable	good
MRI-ESM2-0 historical-ssp585 (1)	good	good	0.634 (0.540 ... 0.747)	good	good	0.0280 (0.0240 ... 0.0330)	reasonable	good
NorESM2-LM historical-ssp585 (1)	reasonable	good	0.838 (0.721 ... 0.997)	good	good	0.0300 (0.0260 ... 0.0360)	reasonable	reasonable
NorESM2-MM historical-ssp585 (1)	reasonable	good	1.05 (0.900 ... 1.25)	good	good	0.0310 (0.0260 ... 0.0370)	reasonable	good
UKESM1-0-LL historical-ssp585 (1)	good	good	0.916 (0.779 ... 1.09)	good	good	0.0340 (0.0290 ... 0.0400)	reasonable	good
EC-EARTH3P (1)	good	good	0.771 (0.644 ... 0.863)	good	good	0.0250 (0.0210 ... 0.0280)	good	<not evaluated>
EC-EARTH3P-HR (1)	good	good	0.659 (0.560 ... 0.748)	good	good	0.0270 (0.0210 ... 0.0310)	good	<not evaluated>
HadGEM3-GC31-HM (1)	good	good	0.734 (0.616 ... 0.826)	good	good	0.0280 (0.0230 ... 0.0330)	good	<not evaluated>
HadGEM3-GC31-LM (1)	good	good	0.720 (0.593 ... 0.828)	good	good	0.0320 (0.0270 ... 0.0360)	good	<not evaluated>
HadGEM3-GC31-MM (1)	good	good	0.712 (0.614 ... 0.786)	good	good	0.0330 (0.0270 ... 0.0380)	good	<not evaluated>
CNRM-CM6-1 (1)	good	good	0.640 (0.525 ... 0.733)	good	good	0.0370 (0.0280 ... 0.0450)	good	<not evaluated>

CNRM-CM6-1-HR (1)	good	good	0.769 (0.650 ... 0.873)	good	good	0.0300 (0.0250 ... 0.0340)	good	<not evaluated>

Table 4. Evaluation results for the climate models considered for the attribution analysis of JJA **root zone soil moisture for NHET region**. The table contains qualitative assessments of seasonal cycle and spatial pattern of precipitation and temperature from the models (good, reasonable, bad) along with estimates for dispersion parameter, shape parameter and event magnitude. The corresponding estimates for observations are shown in blue. The seasonal cycles and spatial patterns for soil moisture are also evaluated, whenever available. Based on overall suitability, the models are classified as good, reasonable and bad, shown by green, yellow and red highlights, respectively.

	Temperature			Precipitation			Root zone soil moisture	
Observations			Sigma			Sigma		
E-OBS			0.656 (0.557 ... 0.746)			0.121 (0.101 ... 0.138)		
ERA5			0.654 (0.549 ... 0.739)			0.125 (0.102 ... 0.144)		

Models	Seasonal cycle	Spatial pattern	Sigma	Seasonal cycle	Spatial pattern	Sigma	Seasonal cycle	Spatial pattern
AM2.5C360 amip1871-2021 (10)	reasonable	good	0.838 (0.792 ... 0.880)	good	good	0.0290 (0.0280 ... 0.0310)	<not evaluated>	<not evaluated>
FLOR historical-rcp45 (10)	reasonable	good	0.901 (0.851 ... 0.946)	good	good	0.0240 (0.0230 ... 0.0250)	<not evaluated>	<not evaluated>
ACCESS-CM2 historical-ssp585 (1)	reasonable	good	0.917 (0.779 ... 1.09)	good	good	0.0340 (0.0290 ... 0.0410)	reasonable	good
ACCESS-ESM1-5 historical-ssp585 (1)	reasonable	good	0.963 (0.823 ... 1.14)	good	reasonable	0.0240 (0.0210 ... 0.0290)	reasonable	reasonable
BCC-CSM2-MR historical-ssp585 (1)	reasonable	good	1.19 (1.02 ... 1.43)	good	reasonable	0.0290 (0.0240 ... 0.0340)	reasonable	reasonable
CESM2-WACCM historical-ssp585 (1)	reasonable	good	0.858 (0.738 ... 1.03)	good	good	0.0310 (0.0260 ... 0.0370)	reasonable	reasonable
CESM2 historical-ssp585 (1)	reasonable	good	0.955 (0.816 ... 1.13)	good	good	0.0320 (0.0270 ... 0.0380)	reasonable	good
CMCC-CM2-SR5 historical-ssp585 (1)	reasonable	reasonable	1.09 (0.934 ... 1.31)	good	good	0.0250 (0.0210 ... 0.0290)	reasonable	good
CMCC-ESM2 historical-ssp585 (1)	reasonable	good	1.12 (0.951 ... 1.34)	good	good	0.0280 (0.0240 ... 0.0330)	reasonable	good
CNRM-CM6-1 historical-ssp585 (1)	good	good	0.835 (0.711 ... 1.00)	good	good	0.0220 (0.0180 ... 0.0260)	reasonable	good

CNRM-ESM2-1 historical-ssp585 (1)	good	reasonable	0.687 (0.591 ... 0.818)	good	good	0.0260 (0.0220 ... 0.0310)	reasonable	reasonable
CanESM5 historical-ssp585 (1)	reasonable	good	0.751 (0.642 ... 0.893)	good	good	0.0290 (0.0250 ... 0.0340)	good	good
EC-Earth3-CC historical-ssp585 (1)	good	good	0.865 (0.738 ... 1.03)	good	good	0.0230 (0.0190 ... 0.0270)	good	good
EC-Earth3-Veg-LR historical-ssp585 (1)	good	good	0.778 (0.661 ... 0.928)	good	good	0.0260 (0.0220 ... 0.0300)	good	good
EC-Earth3-Veg historical-ssp585 (1)	good	good	0.874 (0.748 ... 1.04)	good	good	0.0220 (0.0190 ... 0.0270)	good	good
EC-Earth3 historical-ssp585 (1)	reasonable	good	0.930 (0.795 ... 1.10)	good	good	0.0210 (0.0180 ... 0.0260)	good	good
GFDL-ESM4 historical-ssp585 (1)	good	good	0.625 (0.538 ... 0.746)	good	good	0.0240 (0.0210 ... 0.0290)	reasonable	reasonable
HadGEM3-GC31-LL historical-ssp585 (1)	reasonable	good	0.756 (0.640 ... 0.898)	good	good	0.0280 (0.0240 ... 0.0330)	bad	bad
KACE-1-0-G historical-ssp585 (1)	reasonable	bad	1.06 (0.906 ... 1.27)	bad	reasonable	0.0380 (0.0320 ... 0.0440)	reasonable	reasonable
MIROC6 historical-ssp585 (1)	reasonable	bad	0.681 (0.578 ... 0.818)	good	good	0.0220 (0.0190 ... 0.0260)	reasonable	reasonable
MPI-ESM1-2-LR historical-ssp585 (1)	good	good	0.756 (0.646 ... 0.898)	reasonable	good	0.0230 (0.0200 ... 0.0280)	reasonable	reasonable

MRI-ESM2-0 historical-ssp585 (1)	good	good	0.634 (0.540 ... 0.747)	good	good	0.0280 (0.0240 ... 0.0330)	reasonable	good
NorESM2-LM historical-ssp585 (1)	reasonable	good	0.838 (0.721 ... 0.997)	good	good	0.0300 (0.0260 ... 0.0360)	reasonable	reasonable
NorESM2-MM historical-ssp585 (1)	reasonable	good	1.05 (0.900 ... 1.25)	good	good	0.0310 (0.0260 ... 0.0370)	reasonable	reasonable
TaiESM1 historical-ssp585 (1)	reasonable	good	0.969 (0.829 ... 1.16)	good	good	0.0250 (0.0210 ... 0.0300)	reasonable	good
UKESM1-0-LL historical-ssp585 (1)	good	good	0.916 (0.779 ... 1.09)	good	good	0.0340 (0.0290 ... 0.0400)	reasonable	reasonable

5 Multi-method multi-model attribution

Tables 5-8 show probability ratios (PR) and change in intensity (ΔI) calculated from observations and models for the two variables — surface and root zone soil moisture — for both regions, WCE and NHET. Results are shown for the current climate relative to a 1.2°C cooler climate (before anthropogenic climate change).

5.1 WCE region

Table 5. Probability Ratio (PR) and change in intensity of the **2022 JJA average surface soil moisture in the WCE region** between the current climate and the pre-industrial climate, from the observed datasets and the models that passed validation. This event is defined as a 1-in-20 year event based on observations.

Model / Observations	Probability ratio PR	Change in intensity ΔI [%]
ERA5	49 (7.0 ... 6.3e+2)	-9.6 (-14 ... -5.1)
ERA5-Land	17 (3.0 ... 1.8e+2)	-8.0 (-13 ... -3.4)
GLDAS-CLSM	1.0e+7 (1.1e+5 ... 3.1e+10)	-14 (-16 ... -11)
CanESM5 historical-ssp585 (1)	2.2 (0.93 ... 4.1)	-3.3 (-6.7 ... 0.29)
GFDL-CM4 historical-ssp585 (1)	2.1 (0.64 ... 6.9)	-2.1 (-5.7 ... 1.1)
HadGEM3-GC31-LL historical-ssp585 (1)	21 (8.7 ... 50)	-12 (-16 ... -8.1)
HadGEM3-GC31-MM historical-ssp585 (1)	37 (13 ... 1.2e+2)	-17 (-21 ... -11)
MPI-ESM1-2-HR historical-ssp585 (1)	1.7 (0.56 ... 4.9)	-1.6 (-5.1 ... 1.6)
MPI-ESM1-2-LR historical-ssp585 (1)	11 (3.6 ... 34)	-5.4 (-8.1 ... -2.9)
CNRM-CM6-1 (1)	2.3 (0.37 ... 19)	-2.4 (-7.5 ... 2.7)
CNRM-CM6-1-HR (1)	1.0 (0.23 ... 4.1)	-0.10 (-4.6 ... 5.0)
EC-EARTH3P (1)	1.2 (0.20 ... 6.5)	-0.60 (-6.5 ... 5.5)
EC-EARTH3P-HR (1)	3.7 (0.83 ... 17)	-3.9 (-8.4 ... 0.55)

Table 6. Probability Ratio (PR) and change in intensity of the **2022 JJA average root zone soil moisture in the WCE region** between the current climate and the pre-industrial climate, from the observed datasets and the models that passed validation. This event is defined as a 1-in-20 year event based on observations.

Model / Observations	Probability ratio PR [-]	Change in intensity ΔI [%]
ERA5	4.0e+3 (2.8e+2 ... 5.6e+5)	-16 (-19 ... -12)
ERA5-Land	29 (4.3 ... 3.5e+2)	-8.6 (-13 ... -3.9)
GLDAS-CLSM	7.9e+6 (8.2e+4 ... 2.5e+10)	-14 (-16 ... -11)
CESM2-WACCM historical-ssp585 (1)	4.8 (1.7 ... 12)	-2.9 (-4.8 ... -0.95)
CanESM5 historical-ssp585 (1)	2.3 (1.2 ... 4.4)	-1.9 (-3.5 ... -0.32)

EC-Earth3-CC historical-ssp585 (1)	1.1 (0.63 ... 1.9)	-0.41 (-2.2 ... 1.4)
EC-Earth3-Veg-LR historical-ssp585 (1)	0.70 (0.23 ... 1.4)	1.1 (-1.3 ... 4.3)
HadGEM3-GC31-LL historical-ssp585 (1)	5.5 (2.0 ... 13)	-3.6 (-5.7 ... -1.4)
MPI-ESM1-2-HR historical-ssp585 (1)	0.80 (0.28 ... 2.1)	0.86 (-2.9 ... 4.4)
MPI-ESM1-2-LR historical-ssp585 (1)	7.6 (2.9 ... 21)	-5.7 (-9.0 ... -2.9)

5.2 NHET region

Table 7. Probability Ratio (PR) and change in intensity of the **2022 JJA average surface soil moisture in the NHET region** between the current climate and the pre-industrial climate, from the observed datasets and the models that passed validation. This event is defined as a 1-in-20 year event based on observations.

Model / Observations	**Probability ratio PR [-]**	**Change in intensity ΔI [%]**
ERA5	1.5e+2 (13 ... 4.8e+3)	-2.7 (-3.8 ... -1.4)
ERA5-Land	1.7e+2 (18 ... 6.0e+3)	-2.6 (-3.6 ... -1.5)
GLDAS-CLSM	1.4e+11 (2.2e+7 ... ∞)	-4.4 (-5.0 ... -3.7)
AM2.5C360 amip1871-2021 (10)	0.75 (0.46 ... 1.2)	0.14 (-0.068 ... 0.36)
ACCESS-CM2 historical-ssp585 (1)	7.8 (1.9 ... 24)	-0.66 (-1.1 ... -0.19)
ACCESS-ESM1-5 historical-ssp585 (1)	29 (6.8 ... 1.1e+2)	-1.2 (-1.7 ... -0.69)
BCC-CSM2-MR historical-ssp585 (1)	34 (6.1 ... 1.7e+2)	-2.1 (-3.1 ... -1.1)
CanESM5 historical-ssp585 (1)	10 (4.5 ... 22)	-1.6 (-2.3 ... -1.0)
EC-Earth3 historical-ssp585 (1)	0.084 (0.029 ... 0.22)	3.4 (2.6 ... 4.1)
GFDL-CM4 historical-ssp585 (1)	8.6e+2 (1.4e+2 ... 6.5e+3)	-1.9 (-2.4 ... -1.4)
HadGEM3-GC31-LL historical-ssp585 (1)	4.6e+6 (2.3e+5 ... 1.6e+8)	-5.9 (-6.6 ... -5.2)
HadGEM3-GC31-MM historical-ssp585 (1)	1.3e+8 (3.2e+6 ... 1.1e+10)	-8.2 (-9.3 ... -7.1)
INM-CM5-0 historical-ssp585 (1)	45 (9.5 ... 2.4e+2)	-1.3 (-2.0 ... -0.81)
MPI-ESM1-2-HR historical-ssp585 (1)	2.7 (0.81 ... 8.7)	-0.49 (-1.1 ... 0.098)
MPI-ESM1-2-LR historical-ssp585 (1)	33 (7.4 ... 1.4e+2)	-1.1 (-1.6 ... -0.66)
MRI-ESM2-0 historical-ssp585 (1)	1.6 (0.41 ... 4.9)	-0.21 (-0.77 ... 0.36)
NorESM2-LM historical-ssp585 (1)	3.5e+2 (40 ... 2.9e+3)	-3.3 (-4.6 ... -2.2)
UKESM1-0-LL historical-ssp585 (1)	84 (23 ... 3.2e+2)	-2.5 (-3.2 ... -1.7)
EC-EARTH3P-HR HighResMIP (1)	56 (8.1 ... 7.6e+2)	-1.4 (-2.1 ... -0.72)
HadGEM3-GC31-HM HighResMIP (1)	1.1e+7 (3.0e+5 ... 1.4e+10)	-8.0 (-9.2 ... -6.6)
HadGEM3-GC31-LM HighResMIP (1)	3.3e+6 (7.7e+4 ... 7.2e+9)	-7.4 (-8.7 ... -6.1)
HadGEM3-GC31-MM HighResMIP (1)	3.7e+5 (9.9e+3 ... 3.5e+8)	-6.9 (-8.6 ... -5.2)

CNRM-CM6-1 HighResMIP (1)	8.0e+3 (3.3e+2 ... 7.4e+6)	-2.4 (-3.1 ... -1.8)
CNRM-CM6-1-HR HighResMIP (1)	21 (2.2 ... 4.9e+2)	-1.1 (-1.8 ... -0.27)

Table 8. Probability Ratio (PR) and change in intensity of the **2022 JJA average root zone soil moisture in the NHET region** between the current climate and the pre-industrial climate, from the observed datasets and the models that passed validation. This event is defined as a 1-in-20 year event based on observations.

Model / Observations	**Probability ratio PR [-]**	**Change in intensity ΔI [%]**
ERA5	1.5 (0.38 ... 6.0)	-0.61 (-2.3 ... 1.5)
ERA5-Land	6.5e+2 (39 ... 5.1e+4)	-2.4 (-3.2 ... 1.4)
GLDAS-CLSM	6.2e+9 (1.6e+7 ... 1.9e+15)	-3.1 (-3.6 ... -2.7)
AM2.5C360 amip1871-2021 (10)	0.051 (0.036 ... 0.070)	3.4 (3.2 ... 3.6)
ACCESS-CM2 historical-ssp585 (1)	11 (3.2 ... 37)	-0.52 (-0.83 ... -0.23)
ACCESS-ESM1-5 historical-ssp585 (1)	3.1e+4 (2.9e+3 ... 4.6e+5)	-1.7 (-2.1 ... -1.4)
BCC-CSM2-MR historical-ssp585 (1)	1.1e+4 (1.2e+3 ... 1.2e+5)	-4.0 (-4.9 ... -3.2)
CESM2-WACCM historical-ssp585 (1)	56 (17 ... 1.9e+2)	-1.1 (-1.5 ... -0.77)
CESM2 historical-ssp585 (1)	1.1e+2 (27 ... 4.7e+2)	-1.4 (-1.8 ... -0.94)
CNRM-ESM2-1 historical-ssp585 (1)	2.8e+5 (1.6e+4 ... 6.1e+6)	-2.4 (-2.8 ... -2.0)
CanESM5 historical-ssp585 (1)	48 (17 ... 1.3e+2)	-1.2 (-1.6 ... -0.91)
EC-Earth3-CC historical-ssp585 (1)	0.66 (0.33 ... 1.2)	0.31 (-0.12 ... 0.76)
EC-Earth3-Veg-LR historical-ssp585 (1)	0.42 (0.14 ... 1.0)	0.61 (-0.027 ... 1.3)
EC-Earth3-Veg historical-ssp585 (1)	0.39 (0.17 ... 0.79)	0.56 (0.16 ... 0.95)
EC-Earth3 historical-ssp585 (1)	0.16 (0.056 ... 0.40)	2.1 (1.3 ... 2.9)
GFDL-ESM4 historical-ssp585 (1)	0.39 (0.088 ... 1.4)	0.41 (-0.15 ... 0.98)
HadGEM3-GC31-LL historical-ssp585 (1)	8.8e+2 (1.9e+2 ... 4.6e+3)	-1.9 (-2.4 ... -1.5)
MPI-ESM1-2-HR historical-ssp585 (1)	0.58 (0.17 ... 1.5)	0.31 (-0.26 ... 0.91)
MPI-ESM1-2-LR historical-ssp585 (1)	32 (8.6 ... 1.4e+2)	-1.2 (-1.7 ... -0.73)
MRI-ESM2-0 historical-ssp585 (1)	18 (4.4 ... 67)	-0.96 (-1.5 ... -0.47)
NorESM2-LM historical-ssp585 (1)	4.9e+2 (69 ... 4.9e+3)	-1.7 (-2.3 ... -1.2)
NorESM2-MM historical-ssp585 (1)	74 (11 ... 5.4e+2)	-1.2 (-1.6 ... -0.66)
TaiESM1 historical-ssp585 (1)	30 (6.1 ... 1.3e+2)	-0.90 (-1.3 ... -0.46)

UKESM1-0-LL historical-ssp585 (1)	1.3e+3 (2.7e+2 ... 7.6e+3)	-2.2 (-2.7 ... -1.7)

Similar tables with results for temperature and precipitation for these regions are shown in Appendix Tables A1-A4.

6 Hazard synthesis

For the event definitions described above we evaluate the influence of anthropogenic climate change on the events by calculating the probability ratio as well as the change in intensity using observation-based products (in this case reanalysis data ERA5, ERA-land and GLDAS-CLSM) and climate models. Models which do not pass the validation tests described above are excluded from the analysis. The aim is to synthesise results from models that pass the evaluation along with the observations-based products, to give an overarching attribution statement. **Figs.** 8-11 show the changes in probability (a) and intensity (b) for both regions and both soil moisture depths for the observation-based products (blue) and models (red). To combine them into a synthesised assessment, first, a representation error is added (in quadrature) to the observations, to account for the difference between observations-based datasets that cannot be explained by natural variability. This is shown in these figures as white boxes around the light blue bars. The dark blue bar shows the average over the observation-based products. Next, a term to account for intermodel spread is added (in quadrature) to the natural variability of the models. This is shown in the figures as white boxes around the light red bars. The dark red bar shows the model average, consisting of a weighted mean using the (uncorrelated) uncertainties due to natural variability plus the term representing intermodel spread (i.e., the inverse square of the white bars). Observation-based products and models are combined into a single result in two ways. Firstly, we neglect common model uncertainties beyond the intermodel spread that is depicted by the model average, and compute the weighted average of models (dark red bar) and observations (dark blue bar): this is indicated by the magenta bar. As, due to common model uncertainties, model uncertainty can be larger than the intermodel spread, secondly, we also show the more conservative estimate of an unweighted, direct average of observations (dark red bar) and models (dark blue bar) contributing 50% each, indicated by the white box around the magenta bar in the synthesis figures.

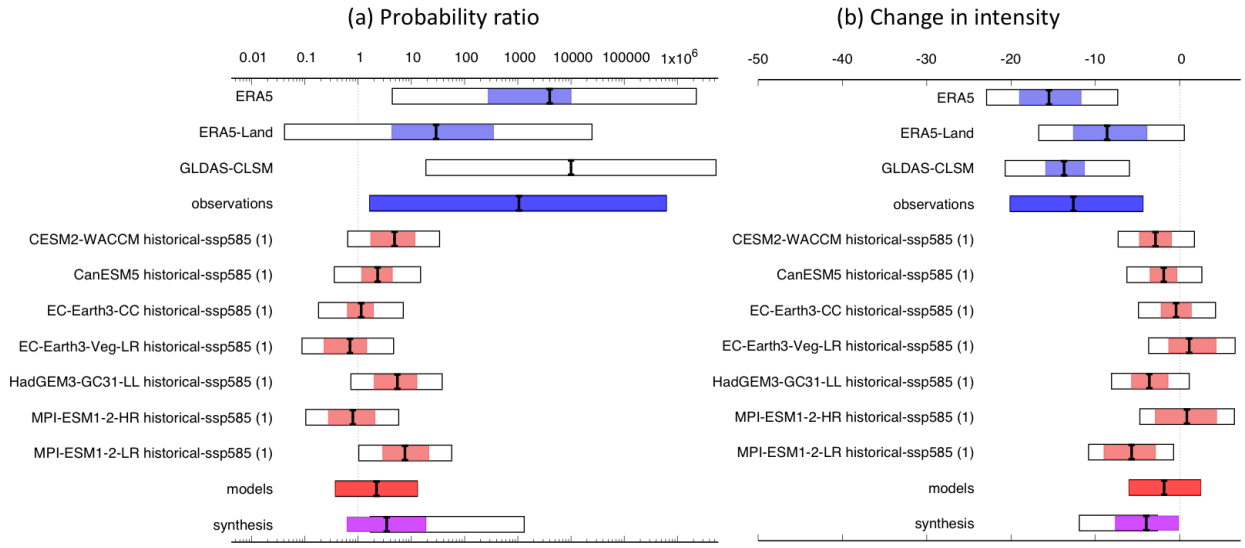

Fig. 8: Synthesis of (a) probability ratios and (b) intensity changes (%) when comparing the return period and magnitudes of the 2022 JJA root zone soil moisture for the WCE region in the current climate and a 1.2ºC cooler climate.

For the root-zone soil moisture over the WCE region the synthesised probability ratio (**Fig. 8**(a)) using the weighted average is PR= 3.4 (0.62 to 19) whereas the unweighted upper bound is much larger at 1300 and the lower bound is also above 1. We therefore use the rounded best estimate as the synthesised result, suggesting anthropogenic climate change has increased the likelihood of the WCE root zone soil moisture event by a factor of 3-4.
The change in intensity for the same event is shown in **Fig. 8**(b) suggesting a change in intensity of -3.9% (-7.60 to -0.13%).

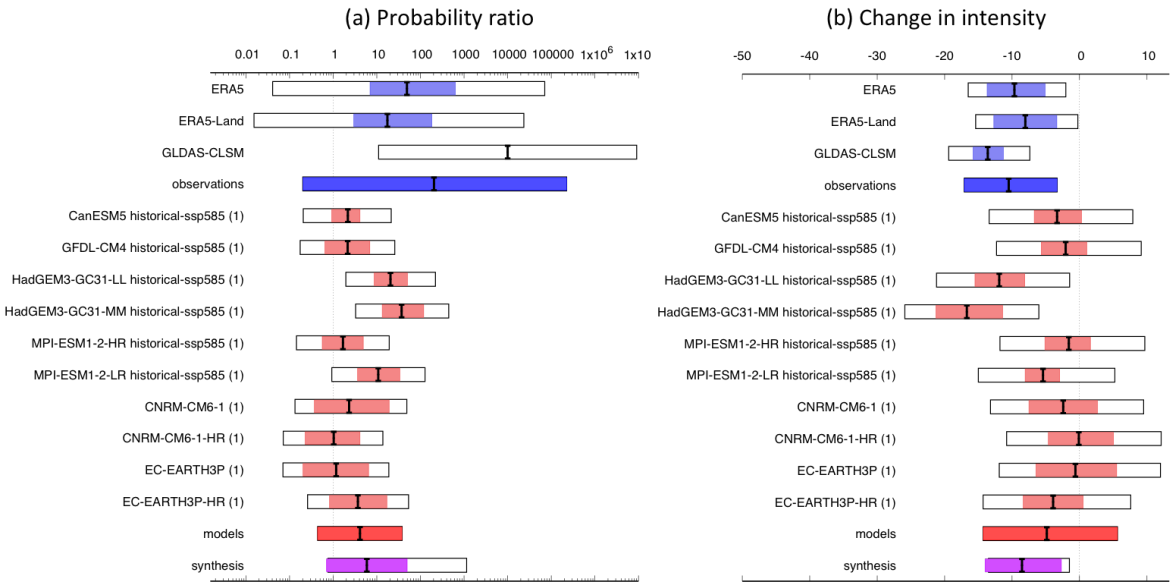

Fig. 9: Synthesis of (a) probability ratios and (b) intensity changes (%) when comparing the return period and magnitudes of the 2022 JJA surface soil moisture for the WCE region in the current climate and a 1.2°C cooler climate.

For the surface soil moisture over the WCE region the synthesised probability ratio using the weighted average is PR= 5.9 (0.71 to 50): whereas the unweighted upper bound is again much larger at 1150, the lower bound in this case is similar to the weighted average, as shown in **Fig. 9**(a). Again we use the rounded best estimate as the synthesised result, suggesting anthropogenic climate change has increased the likelihood of the WCE surface soil moisture event by a factor of 5-6.
The change in intensity for the same event is shown in **Fig. 9**(b) indicating a change in intensity of -8.7% (-14 to -2.7%).

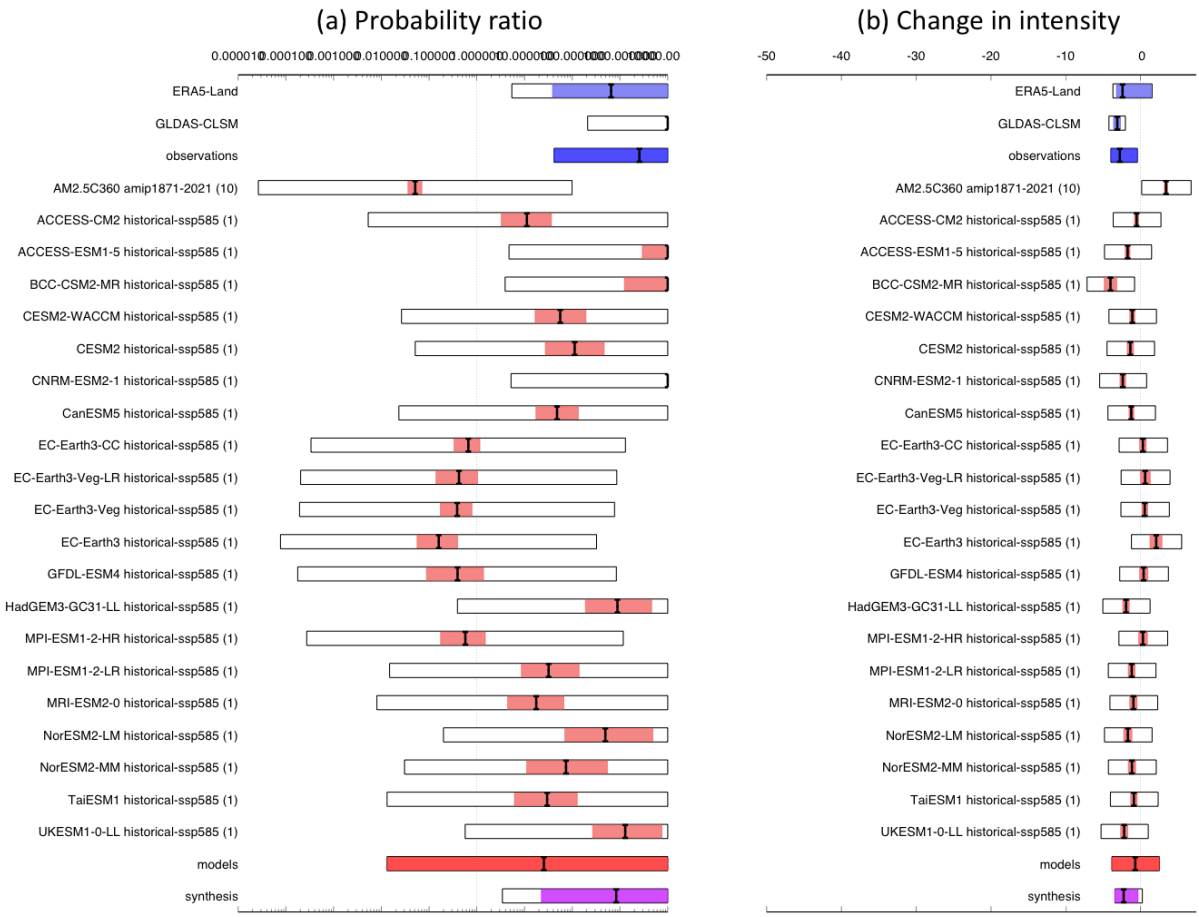

Fig. 10: Synthesis of (a) probability ratios and (b) intensity changes (%) when comparing the return period and magnitudes of the 2022 JJA root zone soil moisture for the NHET region in the current climate and a 1.2°C cooler climate.

For the root zone soil moisture over the NH region the synthesised probability ratio using the weighted average is much larger than for the WCE region with a PR = 860 (23 to 38000) whereas the unweighted upper bound is equally large while the lower bound in this case is lower at a PR of 4, as shown in **Fig. 10**(a). As for a very large probability ratio like this the exact quantification of the best estimate is highly uncertain, we use the lower bound as the synthesised result, suggesting anthropogenic climate change has increased the likelihood of the NH root zone soil moisture event by a factor of at least 20.
The change in intensity for the same event is shown in **Fig. 10**(b) suggesting a change in intensity of -2.3% (-3.4 to -0.34%).

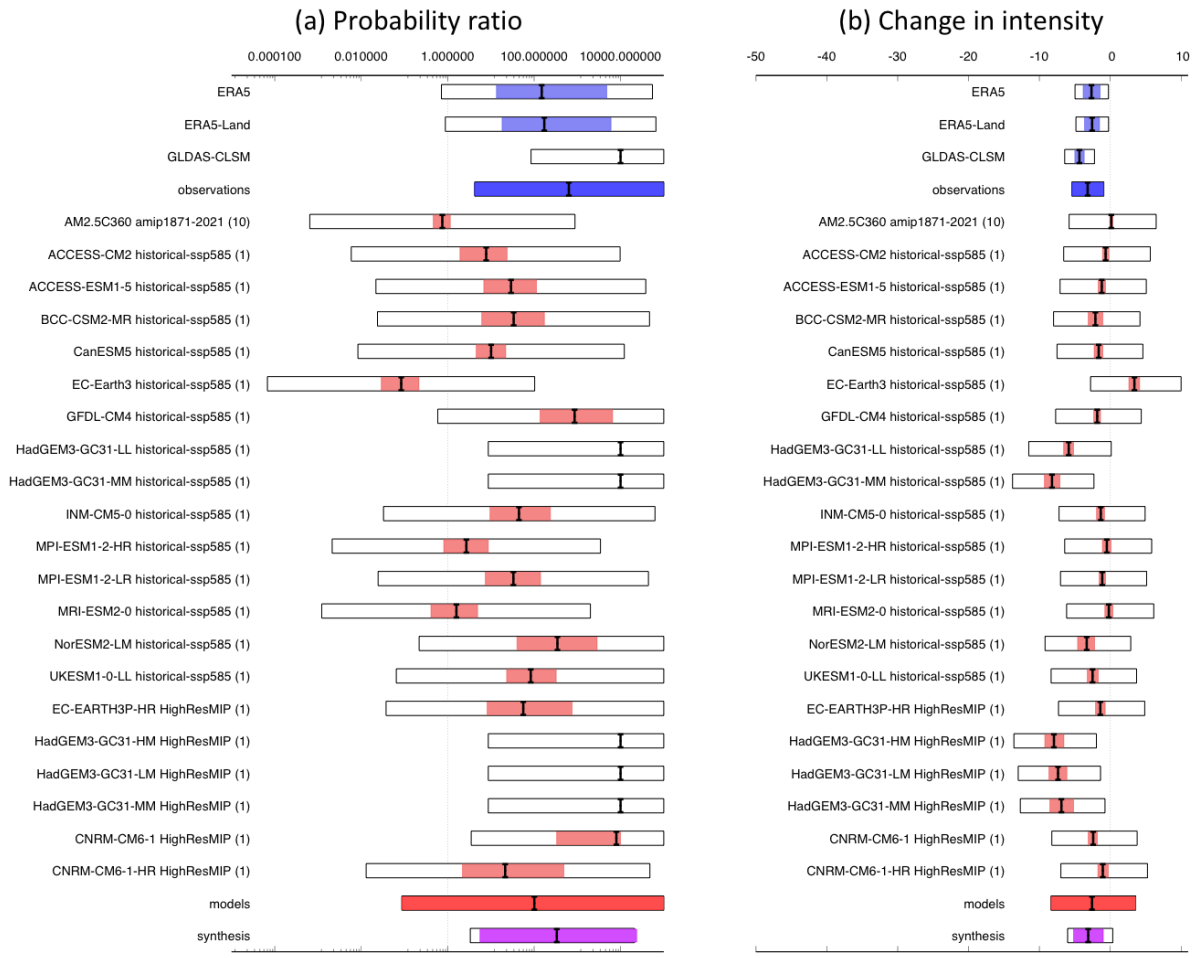

Fig. 11: Synthesis of (a) probability ratios and (b) intensity changes (%) when comparing the return period and magnitudes of the 2022 JJA surface soil moisture for the NHET region in the current climate and a 1.2°C cooler climate.

For the surface soil moisture over the NH region the synthesised probability ratio using the weighted average is again much larger than for the WCE region with a PR = 450 (5 to 44000) and the unweighted bounds are very similar, as shown in **Fig. 11**(a). As for the root zone soil moisture we use the lower bound as the synthesised result, suggesting anthropogenic climate change has increased the likelihood of the NH surface soil moisture event by a factor of at least 5.
The change in intensity for the same event is shown in **Fig. 11**(b) suggesting a change in intensity of -3.3% (-5.7 to -0.85%).

We also looked at the changes in precipitation and temperature over the same timeframe in both regions (Figs. A5-A8). Using the same synthesis procedure the weighted average for temperature in the WCE region is PR = 2430 (214–26400) with a change in intensity of 1.8 (1.1 to 2.5) °C, as shown in Appendix Fig. A5. For the NH region, the probability ratio is statistically indistinguishable from infinity, confirming the finding from the observational analysis that the extreme temperatures over the NH region would have been virtually impossible without climate change. The change in intensity is 1.8 (1.4 to 2.2) °C, as shown in Appendix Fig. A7and thus very similar to the result for WCE. These changes in temperature also show a much larger increase in likelihood over the large region and can thus largely explain the difference in the soil moisture likelihood changes between both regions. The change in precipitation is centred around 1 for both regions (results for temperature and precipitation in Appendix Figs. A6 and A8, respectively) with equally no changes in intensity.

We also assessed how the frequency and intensity of the two types of soil moisture drought in both regions would change in a 0.8°C warmer world compared to today. For all event definitions a further

increase in intensity as well as a 2-30 times further increase in the frequency of such an event is found (Appendix Figs. A9-A12). In combination with the strong trends in temperature extremes these results strengthen our confidence in the soil moisture results, even though an exact quantification is difficult due to the difficulties in measuring soil moisture and resulting large discrepancies in observation-based data sets.

To summarise, synthesising model and observation-driven data, we see that human-induced climate change has increased the probability of the summer 2022 soil moisture drought both in West-Central Europe and in the Northern Hemisphere extratropics. We note that the employed observation-based datasets generally depict a stronger signal than the models, particularly for root-zone soil moisture. Nevertheless, for West-Central Europe and despite considerable uncertainty, we find that a root-zone soil moisture drought has become about 3 to 4 times more likely, and about 5–6 times only for the surface. For the Northern Hemisphere extratropics, the signal is stronger and hence we communicate the far more conservative lower bounds rather than best estimates; for surface soil moisture, human-induced global warming has made an event like in 2022 at least 5 times more likely, whereas for the root-zone soil moisture, the factor is at least 20.

7. Vulnerability and exposure

As of 10 August, nearly two-thirds of Europe was affected by drought (Seabrook, 2022). Extreme dry and hot conditions act as a risk multiplier for energy, environmental and socio-economic vulnerability across Europe (Rakovec et al., 2022; Gazol and Camarero, 2022; Naumann et al., 2021). However, Europe is merely one of many regions across the Northern Hemisphere to suffer from persistent drought and heatwaves as of late.

Southwestern US and Northern Mexico were also experiencing their driest period in more than 1,200 years, causing three water reservoirs, which provide the region with 60 percent of its water, to have drained (Linthicum, 2022). This has led to water insecurity for roughly five million residents in northern Mexico and a disrupted water supply for up to 7.9 million Texas residents (Singh, 2022; Linthicum, 2022). China, particularly Hunan Province, also belongs to the list of the most impacted regions in 2022 as the nation experienced its longest drought and the world's most severe heatwave to date (China Meteorological Administration, 2022; BBC, 2022; Le Page, 2022). The following is an elaboration of the vulnerability and exposure context for the West Central Europe portion of this study.

7.1. Preceding heatwave in Europe

Since the beginning of May to mid-September, five back-to-back heatwaves blanketed large swathes of Europe. Throughout these months, several daily and monthly maximum temperature records were shattered across Italy, France, Switzerland, Germany, Poland, Hungary, and Slovenia (see e.g. Phys.org, 2022; Breteau, 2022; Le News, 2022; Wang, 2022; Twoja Pogoda, 2022; Országos Meteorológiai Szolgálat, 2022; BBC Weather, 2022). An attribution study by Happé et al. (2022) shows that human-induced climate change made the 2022 June heatwave in Spain and France were at least 100, and 10 times more likely, respectively, while the intensity increased by 4 and 3 degrees celsius.

It is estimated that the persistent heat has led to over 24.000 fatalities across Europe, more than 18.000 of which within Western Central Europe - 11.000 in France and over 8.000 in Germany alone (Roucaute, 2022; Destatis, 2022a; Destatis, 2022b). Infrastructure was impacted as the heat melted roads, buckled railway lines, halted public transportation services, and increased the electricity demand while power stations operated at reduced capacity (Vox, 2022; Binnie and Twidale, 2022; Rocha, 2022). Even if global warming is kept below the 1.5°C target, research shows that additional costs in operation and maintenance of roads and railways across the EU would reach up to €0.9 billion. This would rise to €1.3 billion if global temperature rise would r reach 2°C (Mulholland and Feyen, 2021).

By 24 September, more than 770.000 hectares of land had burnt throughout the European Union (EU) (European Forest Fire Information System [EFFIS], 2022), which equals nearly three times the EU average over 2006-2021 (Copernicus, 2022). Italy, Slovenia, France, and Romania were particularly affected by these fires (Roscoe, 2022; Gironde, 2022; ARSO, 2022; Dumitrescu, 2022), and by late June, Italy had crushed its historical wildfire average threefold (The Local, 2022).

7.2. Exposed and impacted agricultural production

Europe's prolonged hot and dry weather conditions during the first half of 2022, and ensuing low water reservoir levels, has led to significant reductions in summer crop yields, most significantly in France, northern Italy, Germany, Slovenia, Hungary, and Romania (EU Science Hub, 2022). These significant agricultural impacts are unsurprising, given the sector is the most water intensive industry in the region (Heggie, 2022; European Environment Agency, 2020). Compared to their five-year averages, maize, soybean and sunflower crops suffered 16, 15 and 12 percent decreases, respectively (European Union, 2022).

In northern Italy, the Po River basin experienced its worst water crisis in approximately 70 years, leading to an estimated 30 percent reduction of rice crop yields and at least 50 cattle deaths (Clifford, 2022; Coldiretti, 2022). Similarly, some crop yields in Germany could face a 40 percent reduction (DW, 2022). Similarly, France's corn harvest is anticipated to decrease by over 18 percent compared to 2021. (VOA News, 2022; RFI, 2022). Paired with the Ukraine crisis hiking up the price for fertilizers fourfold, these decreases in agricultural production are leading to a "heatflation" of food prices as well as higher feed prices for livestock (DW, 2022; Trade Finance Global, 2022). This is expected to result in increased food prices around the world (SP Global, 2022). In turn, this is likely to exacerbate countries' and households' economic strain following Europe's energy crisis.

7.3. Vulnerable energy systems and compound causes of an energy crisis

The drought in Europe also results indirect impacts on electricity generation in many Western European countries (IEA, 2021). Lower river flows and thus lower reservoir levels have significantly decreased hydroelectric power generation. For example, in Italy, hydroelectric plants generated 40-50 percent less power over the summer months, and one plant in Piacenza was temporarily shut down[1]. The low water levels in rivers in Germany also reduced the ability to transport coal by boat, further impacting energy supply (NY Times). In countries like France which relies on nuclear energy (which comprises over 70% of its energy mix), decreased water availability has impacted the ability to safely cool-down nuclear power plants, leading to reduced output and shutdown of nuclear reactors on the Belgium-France border[2][3]. These supply constraints coincided with high demand, particularly due to airconditioning during hot periods.

The drought event came at a time when Europe was facing a number of other, compounding stressors on its energy supply. The COVID-19 pandemic led to a slow-down in demand for energy in 2020, but demand has rebounded by 2022 while supply has not kept up, leading to an increase in global energy prices. In addition, the war in Ukraine has strained ties between Europe and Russia, until recently the main supplier of Europe's natural gas. Russia reduced the supply of natural gas through Nord Stream 1

[1] https://www.euronews.com/2022/08/08/nothing-left-in-the-pipes-europe-tackles-unprecedented-water-shortages-as-heatwave-rages

[2] https://www.rfi.fr/en/france/20200825-drought-provokes-shutdown-nuclear-reactors-northeast-france-belgium-ardennes-chooz-meuse

[3] https://www.theguardian.com/business/2022/aug/03/edf-to-reduce-nuclear-power-output-as-french-river-temperatures-rise

by 75% in June 2022, shut it completely for 10 days in July[4] due to "maintenance" needs, and most recently the pipeline has been shutdown all together due to a leak in the pipeline[5]. The restricted supply has sent prices soaring.

In response to these various pressures on energy supply and demand, the EU is working with its member states to cut demand by 15% between August 2022 and March 2023[67]. It is also using other options, including reopening coal fired power plants, and increasing oil imports in order to avoid an energy shortfall in the coming winter (Nature 2022). This, however, threatens Europe's climate pledge to reduce emissions by 45% by 2030 in order to limit warming to 1.5°C as agreed to in the Paris Agreement (Nature, 2022). Crucially, alternative energy sources could help to substitute for around 70% of gas imports from Russia in case of temporary disruptions (up to 6 months).[8]

The impact of the energy crisis is still unfolding and different countries within Europe will feel different effects based on their energy mix, and import capacity from alternative routes. For Germany, the ongoing energy crisis has far-reaching economic ramifications affecting small and medium-sized enterprises, the backbone of Germany's economy (Kagerl et a., 2022).

7.4. Vulnerable water infrastructure and unsustainable water use

Roughly 66 percent of the European population relies on groundwater for its water-related needs, and about 60 percent are residing in cities where groundwater is over-exploited (European Environmental Agency, 2020). Only topped by the Swiss, at 300 liters per household, Italians use an average of 220 liters which is ten times more water than what is required to meet basic human needs (EurEau, 2020). Beyond exacerbating the risk of water shortages, water leakages and unsustainable water use are driving the loss of European wetlands, which in turn limits drinking water supplies, reduces biodiversity, and decreases natural flood buffers (European Environmental Agency, 2020).

In the EU, water wastage in public supply systems is estimated to total at 20-40 percent of available water, but individual cities throughout the continent are found to experience losses of up to 80 percent (European Environment Agency, 2020; Hirschnitz-Garbers et al., 2016). Specifically in Italy, for example, the poor water distribution system leads the national average of water loss to reach 40 percent (Heggie, 2020). One-third of Italy's urban centres, where water demand typically peaks, is experiencing even greater leakages of up to 45 percent (Bonnel, 2022).

The drought highlighted these gaps and their danger. By early August of this year, over 100 French municipalities were short on potable tap water and relied on water deliveries by truck (Chadwick, 2022). To effectively conserve water, multiple countries enforced water protection practices. Cities and districts across Germany prohibited extraction from various bodies of water, as well as filling pools, watering lawns, and cleaning cars (Stresing and Wolf, 2022). Similarly, some of the most populous urban centres in Italy, including Verona and Pisa, introduced water rationing, stating that tap water was only to be used for domestic use and hygiene purposes (Euronews, 2022a; DW, 2022). Finally, as 62 of 96 of France's departments were at the highest level of drought alert, the majority of which implemented water restrictions (Al Jazeera, 2022). While the country experienced its driest July in more than half a decade (BBC, 2022), and its reportedly most extreme drought in history (The New York Times, 2022), the effects of the below-average rainfall is likely to have been aggravated by leaking water distribution systems across the region.

---

[4] Statistica, 2022: https://de.statista.com/statistik/daten/studie/1316029/umfrage/russischer-gasexport-nach-deutschland-auf-tagesbasis/

[5] https://www.bbc.com/news/world-europe-60131520

[6] https://www.bbc.com/news/business-62305094

[7] https://ec.europa.eu/commission/presscorner/detail/en/IP_22_3131

[8] https://www.elibrary.imf.org/view/journals/001/2022/145/article-A001-en.xml

A key challenge in dealing with rising water stress is how to allocate water among competing priorities. For instance, a country like the Netherlands, often praised for its proactive water management when it comes to handling the risk of excess amounts of water, is facing challenges handling the trade-offs between regions and various types of users, as well as between the ability to manage extreme downpours as well as extended periods of drought (Kuks et al. 2022).[9]

7.5. Risk planning

As described above, the impacts of this drought were multifaceted and highlighted key vulnerabilities in Europe's agriculture, energy, and water management practices.

Until recently drought risk management at the pan-European scale has predominantly focused on coping with financial losses, mainly through calamity funds, mutual funds, and insurances (Diaz-Caneja et al., 2009). Nevertheless, today's scientific consensus points to the need to move from a reactive to a proactive risk management strategy (Wilhite et al., 2007; Blauhut et al., 2016).

Blauhut et al. 2022 notes that drought risk management planning does not exist in a unified continental scale in Europe, despite the potential benefits for large scale directive planning in reducing emergency response costs. Following a comprehensive review of drought management practices in 28 European countries and surveyed 712 experts across Europe, the paper recommends some key areas to reduce vulnerability and exposure from the planning perspective. Its recommendations include developing a pan-European approach to drought management, that allows for country contextualization while also supporting cross-border drought preparedness efforts. In Central and Southern Europe for example, it also recommends a need for greater resourcing, enforcement and technical guidance from government authorities.

7.6. V&E Conclusion

The heat and drought in Western Central Europe had far-reaching impacts on a variety of sectors including health, energy, agriculture, and municipal water supply, reflecting the need to reassess drought preparedness and deal with trade-offs in water management.. It came at a time when its impacts were interacting with non-climate risks to create compounding and cascading impacts. For example, impacts on power generation due to heat and drought (on hydropower, nuclear and coal powerplants) coincided with increasing energy prices linked to the conflict in Ukraine. Similarly, impacts on agricultural yields in Europe coincided with strained global food supply due to reduced exports from Russia and Ukraine, as well as high fertilizer prices with knock-on effects on inflation in Europe, but also on global food prices and therefore food insecurity, resulting in risks cascading across sectors and regions (as flagged as a rising risk in IPCC AR6 WGII (IPCC 2022))

Data availability

Almost all data are or will soon be available via the Climate Explorer.

Acknowledgements

This analysis was partly funded by the XAIDA H2020 project, and has received funding from the European Union's Horizon 2020 research and innovation programme under grant agreement No 101003469.

[9] https://journals.sagepub.com/doi/10.1177/1087724X221128814

Appendix Figures

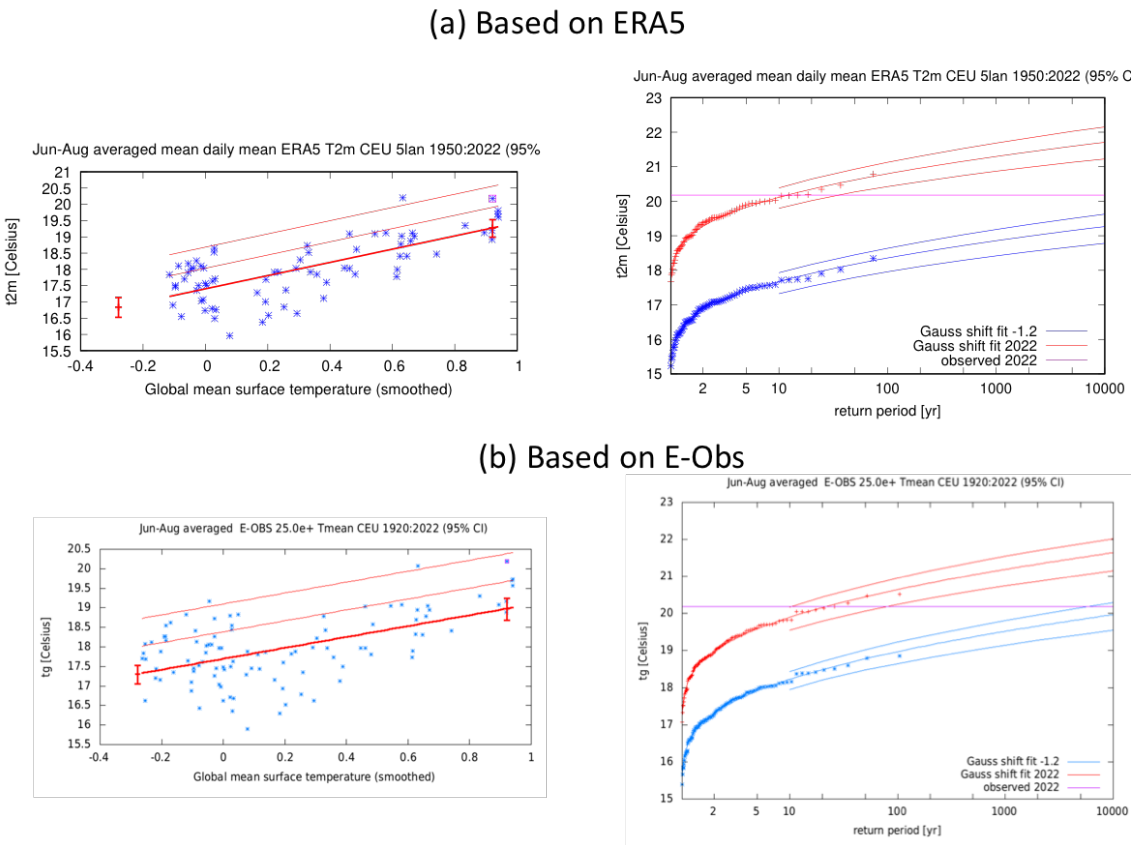

Fig. A1: Gaussian fit with constant dispersion parameter, and the location parameter shifting proportional to GMST of the index series, for the WCE region based on three gridded datasets- (a) ERA5 and (b) E-OBS. The 2022 event is included in the fit. **Left**: Observed JJA average temperature as a function of the smoothed GMST. The thick red line denotes the time-varying location parameter. The vertical red lines show the 95% confidence interval for the location parameter, for the current, 2022 climate and a 1.2ºC cooler climate. The 2022 observation is highlighted with the magenta box. **Right**: Return time plots for the climate of 2022 (red) and a climate with GMST 1.2 ºC cooler (blue). The past observations are shown twice: once shifted up to the current climate and once shifted down to the climate of the late nineteenth century. The markers show the data and the lines show the fits and uncertainty from the bootstrap. The magenta line shows the magnitude of the 2022 event analysed here.

(a) Based on ERA5

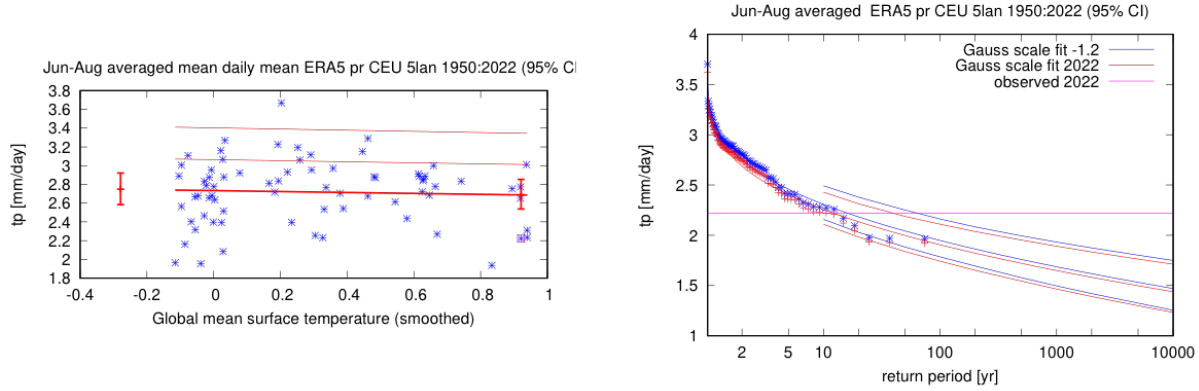

(b) Based on E-Obs

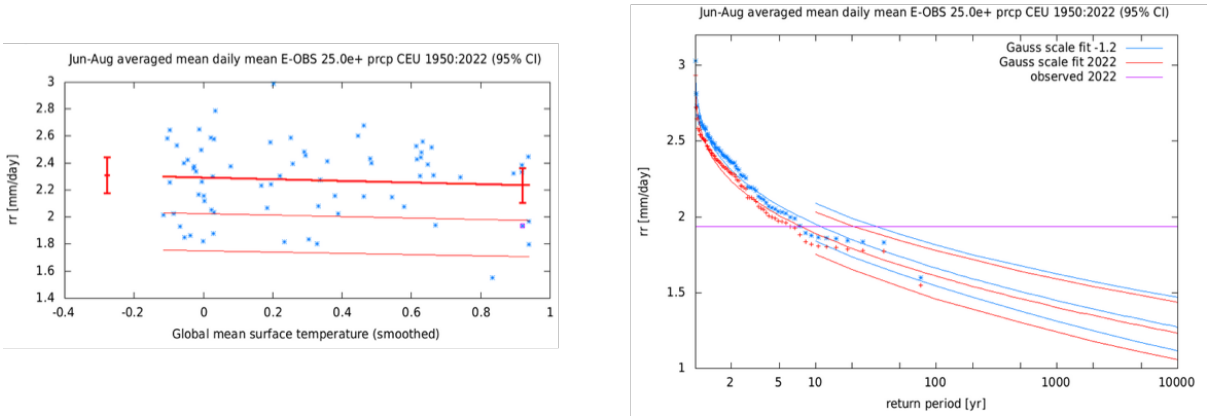

Fig. A2: Gaussian fit with constant dispersion parameter, and the location parameter scaling proportional to GMST of the index series, for the WCE region based on three gridded datasets- (a) ERA5 and (b) E-OBS. The 2022 event is included in the fit. **Left**: Observed JJA average precipitation as a function of the smoothed GMST. The thick red line denotes the time-varying location parameter. The vertical red lines show the 95% confidence interval for the location parameter, for the current, 2022 climate and a 1.2ºC cooler climate. The 2022 observation is highlighted with the magenta box. **Right**: Return time plots for the climate of 2022 (red) and a climate with GMST 1.2 ºC cooler (blue). The past observations are shown twice: once shifted up to the current climate and once shifted down to the climate of the late nineteenth century. The markers show the data and the lines show the fits and uncertainty from the bootstrap. The magenta line shows the magnitude of the 2022 event analysed here.

Based on ERA5

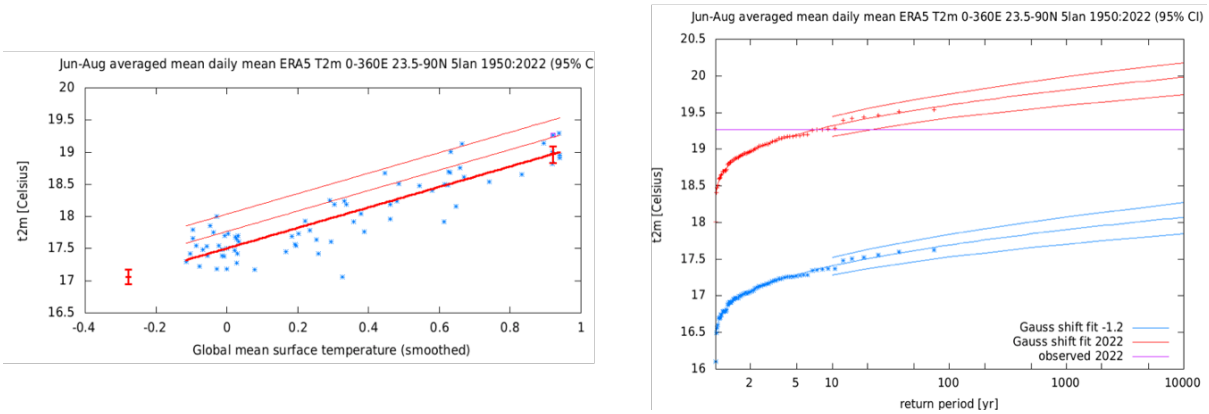

Fig. A3: same as Fig. A1, based on ERA5 dataset for NHET region

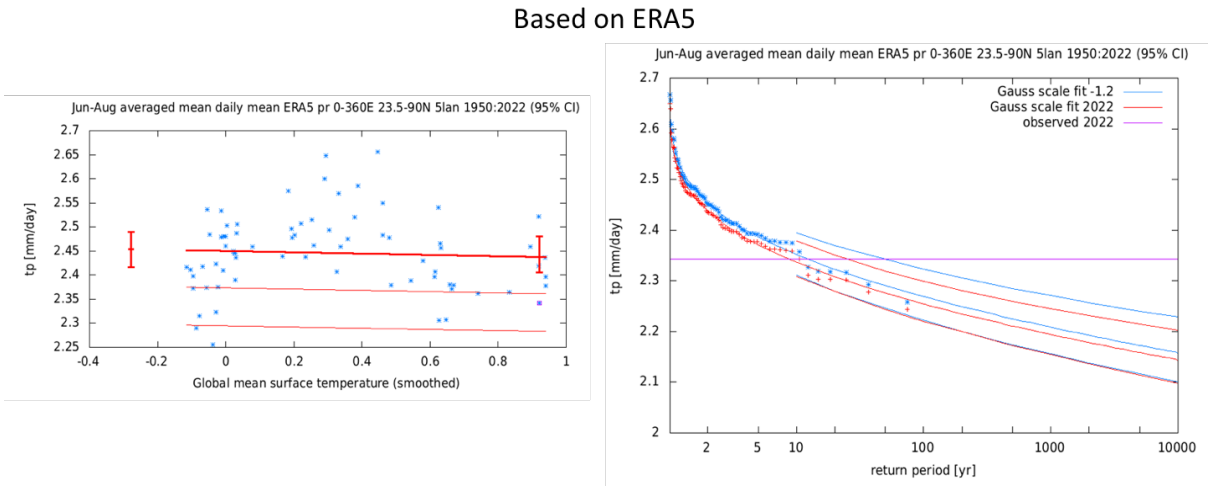

Fig. A4: same as Fig. A2, based on ERA5 dataset for NHET region

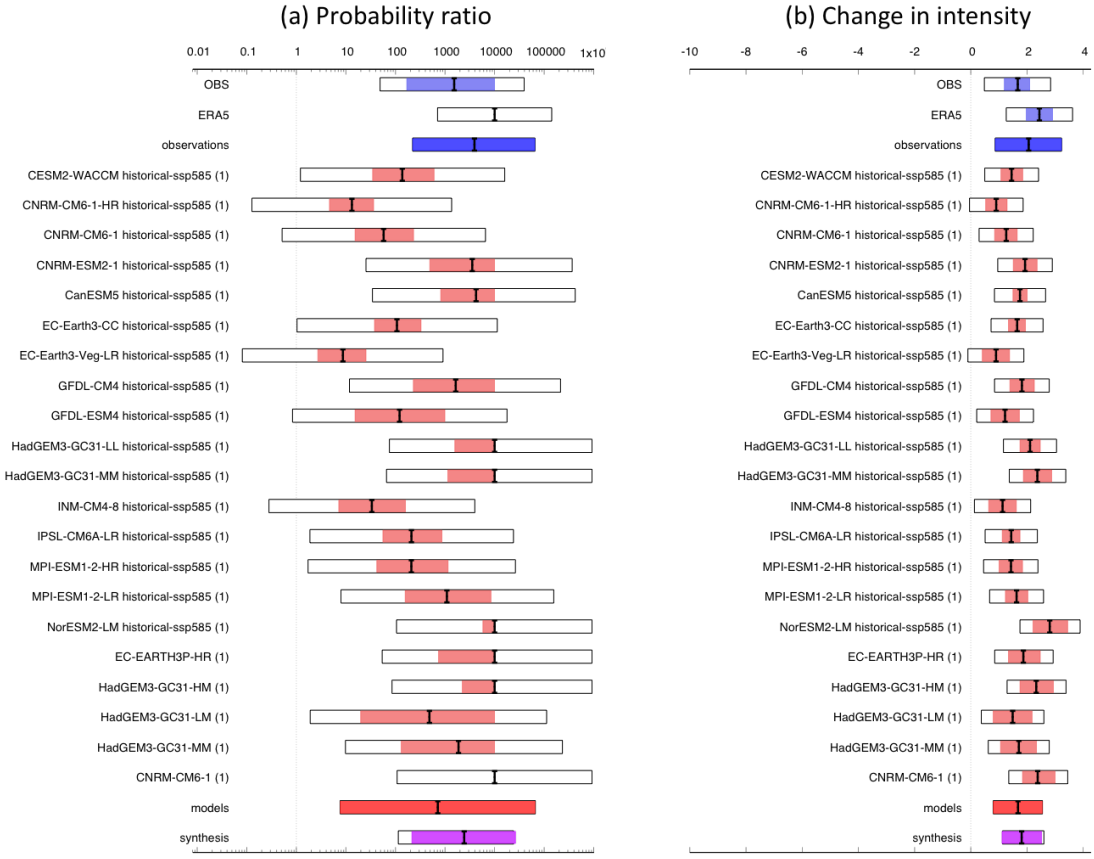

Fig. A5: Synthesis of (a) probability ratios and (b) intensity changes when comparing the return period and magnitudes of the 2022 JJA temperature for the WCE region in the current climate and a 1.2°C cooler climate.

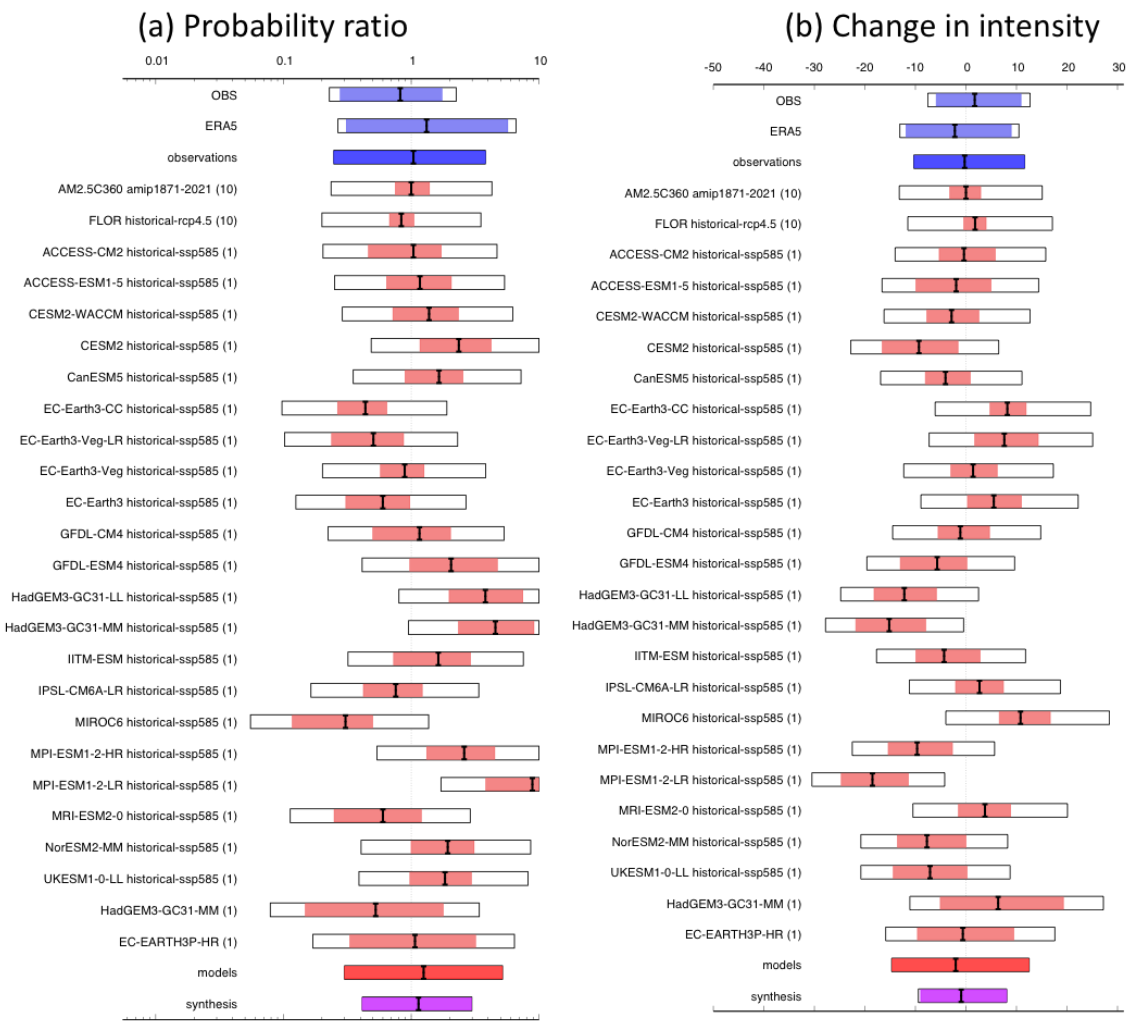

Fig. A6: Synthesis of (a) probability ratios and (b) intensity changes when comparing the return period and magnitudes of the 2022 JJA precipitation for the WCE region in the current climate and a 1.2ºC cooler climate.

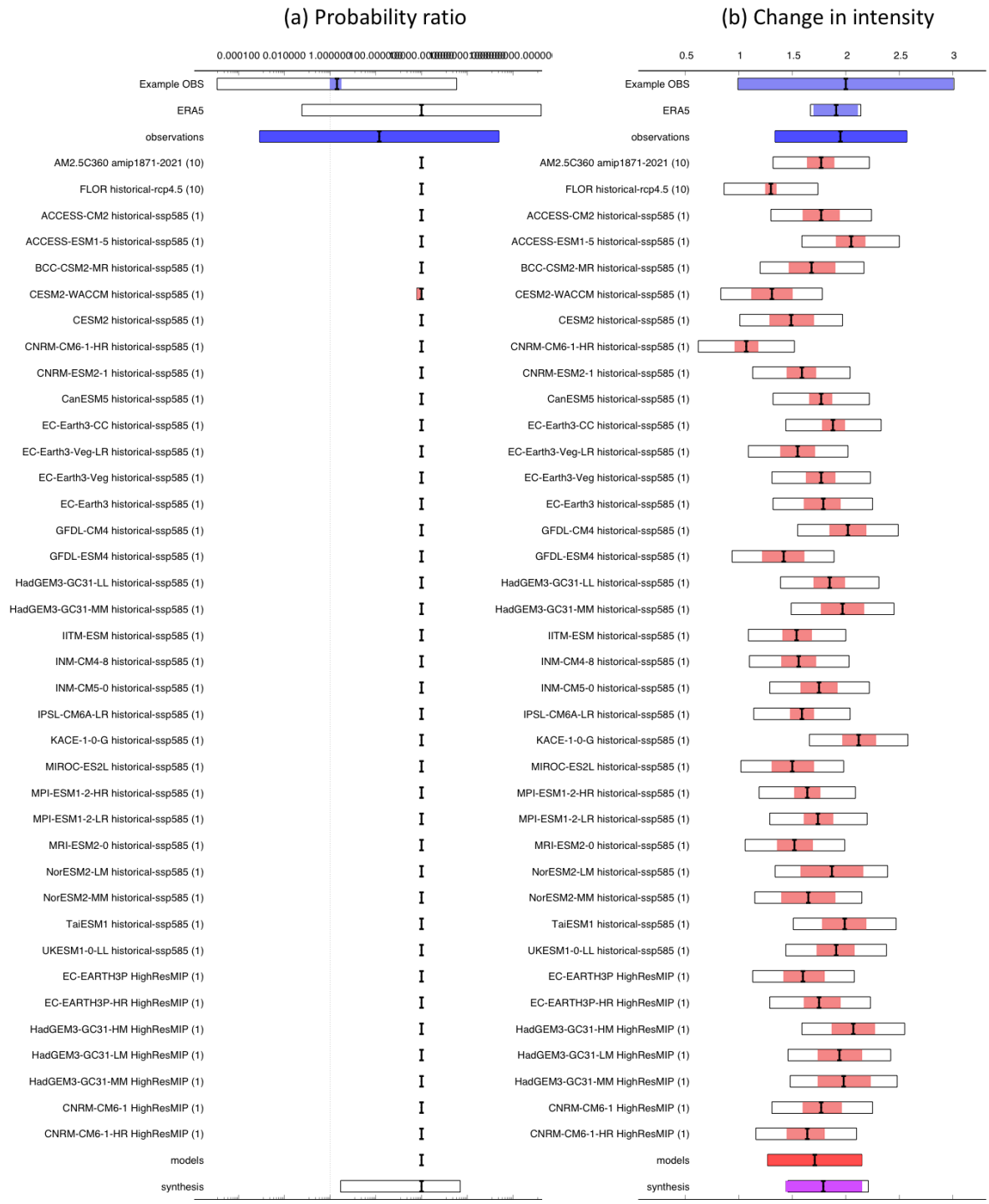

Fig. A7: Synthesis of (a) probability ratios and (b) intensity changes when comparing the return period and magnitudes of the 2022 JJA temperature for the NHET region in the current climate and a 1.2ºC cooler climate.

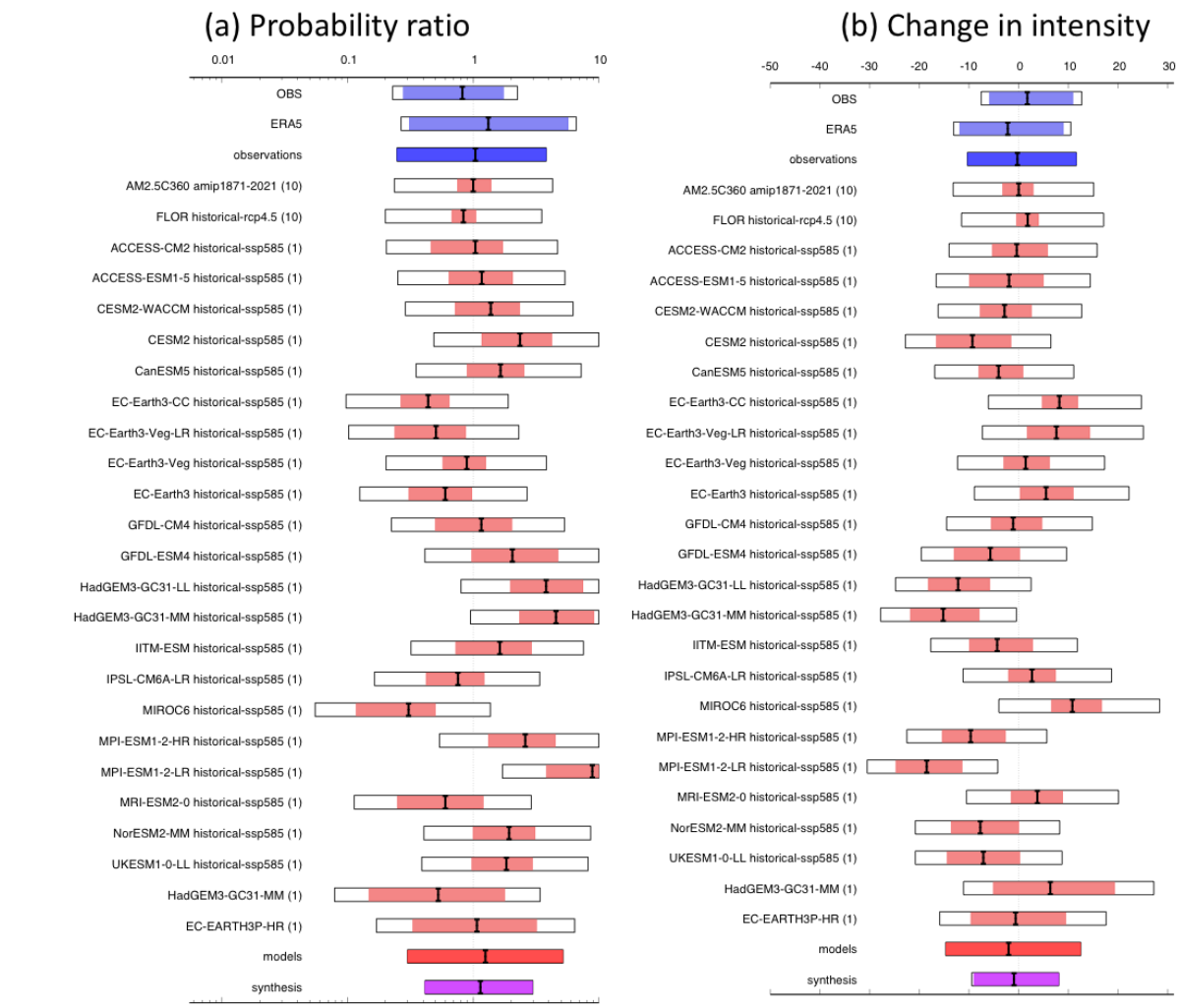

Fig. A8: Synthesis of (a) probability ratios and (b) intensity changes when comparing the return period and magnitudes of the 2022 JJA precipitation for the NHET region in the current climate and a 1.2ºC cooler climate.

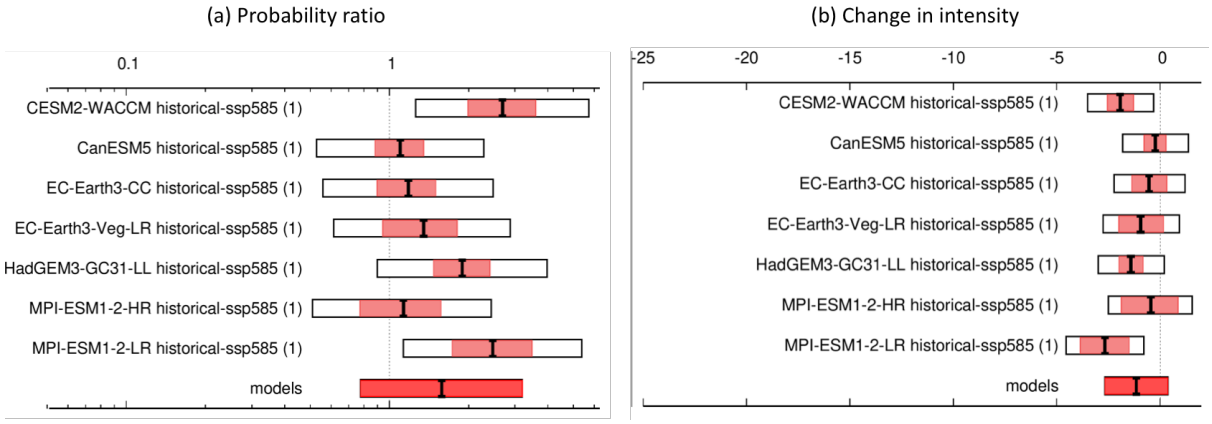

Fig. A9: Synthesis of (a) probability ratios and (b) intensity changes (%) when comparing the return period and magnitudes of the 2022 JJA root zone soil moisture for the WCE region in the current climate and a 1.2ºC cooler climate.

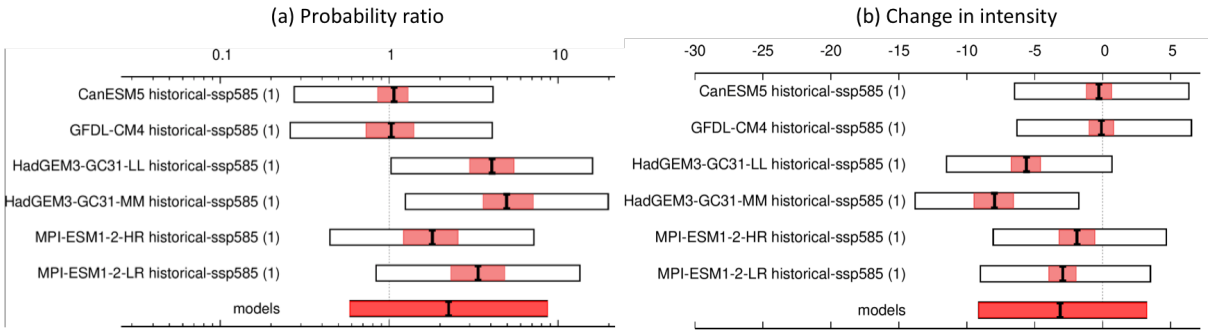

Fig. A10: Synthesis of (a) probability ratios and (b) intensity changes (%) when comparing the return period and magnitudes of the 2022 JJA surface soil moisture for the WCE region in the current climate and a 1.2°C cooler climate.

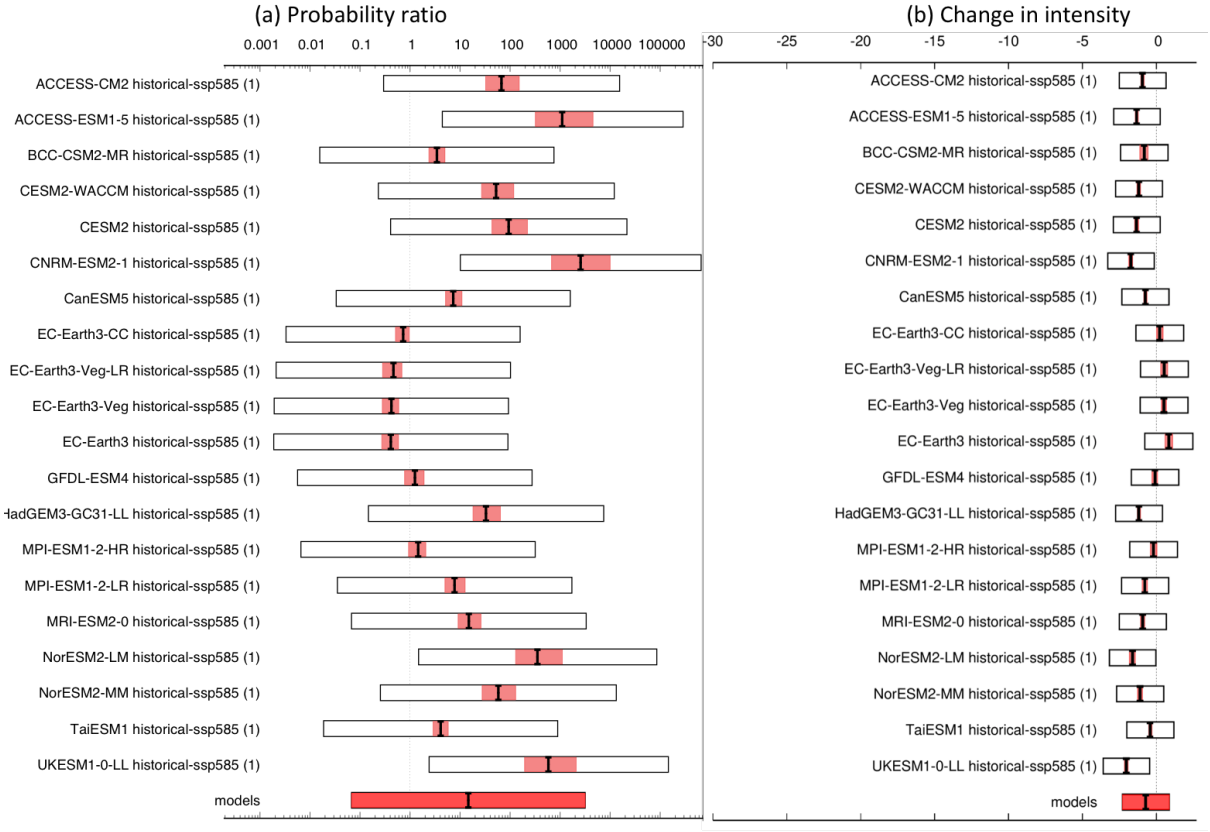

Fig. A11: Synthesis of (a) probability ratios and (b) intensity changes (%) when comparing the return period and magnitudes of the 2022 JJA root zone soil moisture for the NHET region in the current climate and a 1.2°C cooler climate.

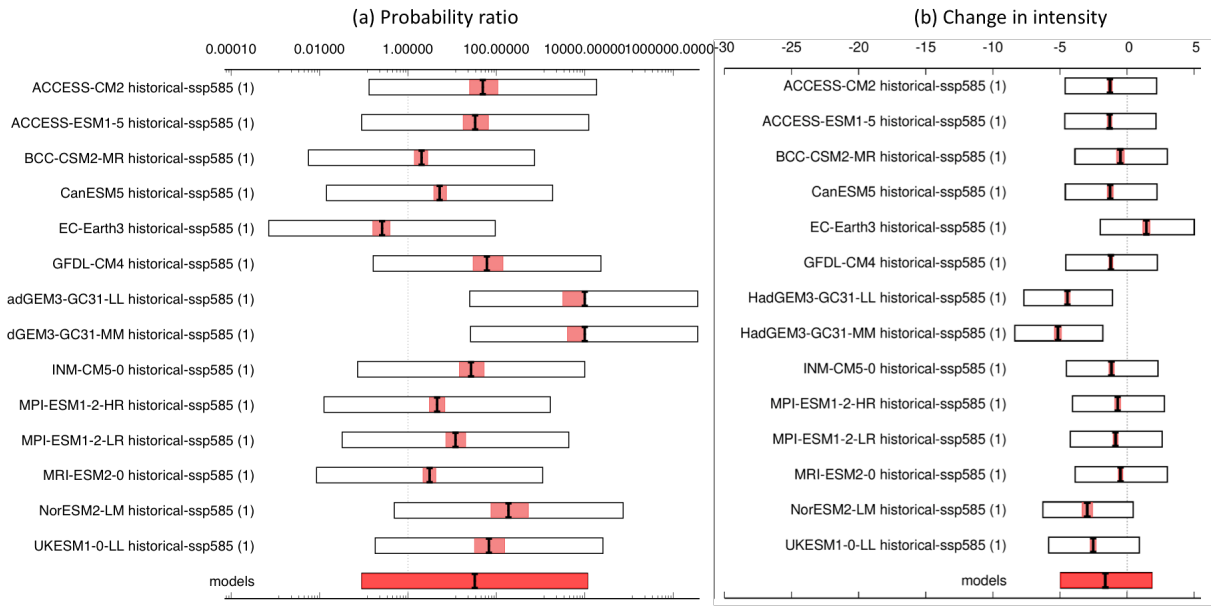

Fig. A12: Synthesis of (a) probability ratios and (b) intensity changes (%) when comparing the return period and magnitudes of the 2022 JJA surface soil moisture for the NHET region in the current climate and a 1.2°C cooler climate.

Appendix Tables

Table A1. Probability Ratio (PR) and change in intensity of the 2022 **JJA average temperature in the WCE region** between the current climate and the pre-industrial climate, from the observed datasets and the models that passed validation. This event is defined as a 1-in-20 year event based on observations.

Model / Observations	Probability ratio PR [-]	Change in intensity ΔI [%]
E-OBS	1.5e+3 (1.7e+2 ... 3.3e+4)	1.7 (1.2 ... 2.1)
ERA5	5.2e+5 (2.2e+4 ... 1.8e+8)	2.4 (2.0 ... 2.9)
CESM2-WACCM historical-ssp585 (1)	1.4e+2 (34 ... 6.0e+2)	1.4 (1.1 ... 1.9)
CNRM-CM6-1-HR historical-ssp585 (1)	13 (4.6 ... 36)	0.91 (0.53 ... 1.3)
CNRM-CM6-1 historical-ssp585 (1)	58 (15 ... 2.3e+2)	1.3 (0.85 ... 1.6)
CNRM-ESM2-1 historical-ssp585 (1)	3.5e+3 (4.9e+2 ... 2.9e+4)	1.9 (1.5 ... 2.4)
CanESM5 historical-ssp585 (1)	4.2e+3 (8.2e+2 ... 2.9e+4)	1.7 (1.5 ... 2.0)
EC-Earth3-CC historical-ssp585 (1)	1.1e+2 (38 ... 3.3e+2)	1.6 (1.3 ... 1.9)
EC-Earth3-Veg-LR historical-ssp585 (1)	8.7 (2.7 ... 25)	0.90 (0.41 ... 1.4)
GFDL-CM4 historical-ssp585 (1)	1.6e+3 (2.3e+2 ... 1.4e+4)	1.8 (1.4 ... 2.3)
GFDL-ESM4 historical-ssp585 (1)	1.2e+2 (15 ... 9.9e+2)	1.2 (0.71 ... 1.7)
HadGEM3-GC31-LL historical-ssp585 (1)	1.1e+4 (1.6e+3 ... 1.1e+5)	2.1 (1.7 ... 2.5)
HadGEM3-GC31-MM historical-ssp585 (1)	1.1e+4 (1.1e+3 ... 1.2e+5)	2.4 (1.9 ... 2.9)
INM-CM4-8 historical-ssp585 (1)	33 (7.2 ... 1.6e+2)	1.1 (0.64 ... 1.6)
IPSL-CM6A-LR historical-ssp585 (1)	2.1e+2 (56 ... 8.7e+2)	1.4 (1.1 ... 1.7)
MPI-ESM1-2-HR historical-ssp585 (1)	2.1e+2 (42 ... 1.1e+3)	1.4 (1.0 ... 1.8)
MPI-ESM1-2-LR historical-ssp585 (1)	1.1e+3 (1.6e+2 ... 8.5e+3)	1.6 (1.2 ... 2.0)
NorESM2-LM historical-ssp585 (1)	1.1e+5 (5.8e+3 ... 2.8e+6)	2.8 (2.2 ... 3.4)
EC-EARTH3P-HR (1)	1.4e+4 (7.4e+2 ... 1.4e+6)	1.9 (1.3 ... 2.5)
HadGEM3-GC31-HM (1)	6.9e+4 (2.2e+3 ... 4.4e+7)	2.3 (1.8 ... 2.9)
HadGEM3-GC31-LM (1)	4.8e+2 (20 ... 9.4e+4)	1.5 (0.80 ... 2.2)
HadGEM3-GC31-MM (1)	1.9e+3 (1.3e+2 ... 1.1e+5)	1.7 (1.1 ... 2.3)
CNRM-CM6-1 (1)	1.2e+6 (2.3e+4 ... 9.2e+8)	2.4 (1.8 ... 3.0)

Table A2. Probability Ratio (PR) and change in intensity of the 2022 **JJA average precipitation in the WCE region** between the current climate and the pre-industrial climate, from the observed datasets and the models that passed validation. This event is defined as a 1-in-10 year event based on observations.

Model / Observations	Probability ratio PR [-]	Change in intensity ΔI [%]

E-OBS	0.82 (0.28 ... 2.0)	1.7 (-5.9 ... 11)
ERA5	1.3 (0.31 ... 5.7)	-2.2 (-12 ... 9.0)
AM2.5C360 amip1871-2021 (10)	1.0 (0.75 ... 1.4)	0.0010 (-3.2 ... 2.9)
FLOR historical-rcp4.5 (10)	0.84 (0.68 ... 1.0)	1.8 (-0.45 ... 4.0)
ACCESS-CM2 historical-ssp585 (1)	1.0 (0.46 ... 1.7)	-0.39 (-5.3 ... 5.8)
ACCESS-ESM1-5 historical-ssp585 (1)	1.2 (0.64 ... 2.1)	-1.9 (-9.9 ... 5.0)
CESM2-WACCM historical-ssp585 (1)	1.4 (0.72 ... 2.3)	-2.8 (-7.8 ... 2.6)
CESM2 historical-ssp585 (1)	2.4 (1.2 ... 4.2)	-9.3 (-17 ... -1.6)
CanESM5 historical-ssp585 (1)	1.6 (0.89 ... 2.5)	-4.0 (-8.0 ... 0.86)
EC-Earth3-CC historical-ssp585 (1)	0.44 (0.27 ... 0.65)	8.2 (4.7 ... 12)
EC-Earth3-Veg-LR historical-ssp585 (1)	0.51 (0.24 ... 0.87)	7.6 (1.7 ... 14)
EC-Earth3-Veg historical-ssp585 (1)	0.89 (0.57 ... 1.3)	1.4 (-3.0 ... 6.2)
EC-Earth3 historical-ssp585 (1)	0.60 (0.31 ... 0.98)	5.5 (0.30 ... 11)
GFDL-CM4 historical-ssp585 (1)	1.2 (0.50 ... 2.0)	-1.1 (-5.5 ... 4.7)
GFDL-ESM4 historical-ssp585 (1)	2.0 (0.97 ... 4.7)	-5.7 (-13 ... 0.19)
HadGEM3-GC31-LL historical-ssp585 (1)	3.8 (2.0 ... 7.5)	-12 (-18 ... -5.8)
HadGEM3-GC31-MM historical-ssp585 (1)	4.6 (2.3 ... 9.1)	-15 (-22 ... -8.0)
IITM-ESM historical-ssp585 (1)	1.6 (0.73 ... 2.9)	-4.3 (-9.9 ... 2.8)
IPSL-CM6A-LR historical-ssp585 (1)	0.76 (0.42 ... 1.2)	2.7 (-2.1 ... 7.4)
MIROC6 historical-ssp585 (1)	0.31 (0.12 ... 0.50)	11 (6.6 ... 17)
MPI-ESM1-2-HR historical-ssp585 (1)	2.6 (1.3 ... 4.5)	-9.7 (-15 ... -2.7)
MPI-ESM1-2-LR historical-ssp585 (1)	8.9 (3.8 ... 20)	-18 (-25 ... -11)
MRI-ESM2-0 historical-ssp585 (1)	0.60 (0.25 ... 1.2)	3.8 (-1.5 ... 8.9)
NorESM2-MM historical-ssp585 (1)	1.9 (1.0 ... 3.1)	-7.7 (-14 ... 0.022)
UKESM1-0-LL historical-ssp585 (1)	1.8 (0.98 ... 3.0)	-7.1 (-14 ... 0.23)
HadGEM3-GC31-MM (1)	0.53 (0.15 ... 1.8)	6.4 (-5.1 ... 19)
EC-EARTH3P-HR (1)	1.1 (0.33 ... 3.2)	-0.62 (-9.6 ... 9.5)

Table A3. Probability Ratio (PR) and change in intensity of the 2022 **JJA average temperature in the NHET region** between the current climate and the pre-industrial climate, from the observed datasets and the models that passed validation. This event is defined as a 1-in-10 year event based on observations.

Model / Observations	**Probability ratio PR [-]**	**Change in intensity ΔI [%]**
Example OBS	2.0 (1.0 ... 3.0)	2.0 (1.0 ... 3.0)
ERA5	5.2e+14 (4.9e+10 ... ∞)	1.9 (1.7 ... 2.1)
	(...)	(...)

AM2.5C360 amip1871-2021 (10)	3.9e+13 (2.8e+11 ... 1.5e+16)	1.8 (1.6 ... 1.9)
FLOR historical-rcp4.5 (10)	9.5e+7 (1.4e+7 ... 9.7e+8)	1.3 (1.2 ... 1.4)
ACCESS-CM2 historical-ssp585 (1)	1.1e+11 (8.0e+8 ... 3.8e+13)	1.8 (1.6 ... 1.9)
ACCESS-ESM1-5 historical-ssp585 (1)	8.6e+19 (1.3e+16 ... 4.6e+24)	2.0 (1.9 ... 2.2)
BCC-CSM2-MR historical-ssp585 (1)	3.5e+8 (6.3e+6 ... 3.9e+10)	1.7 (1.5 ... 1.9)
CESM2-WACCM historical-ssp585 (1)	5.7e+4 (6.2e+3 ... 6.8e+5)	1.3 (1.1 ... 1.5)
CESM2 historical-ssp585 (1)	3.3e+5 (2.4e+4 ... 5.2e+6)	1.5 (1.3 ... 1.7)
CNRM-CM6-1-HR historical-ssp585 (1)	6.7e+6 (3.0e+5 ... 2.1e+8)	1.1 (0.96 ... 1.2)
CNRM-ESM2-1 historical-ssp585 (1)	9.5e+13 (1.7e+11 ... 1.3e+17)	1.6 (1.4 ... 1.7)
CanESM5 historical-ssp585 (1)	3.2e+12 (1.3e+10 ... 1.6e+15)	1.8 (1.7 ... 1.9)
EC-Earth3-CC historical-ssp585 (1)	3.2e+11 (2.1e+9 ... 1.2e+14)	1.9 (1.8 ... 2.0)
EC-Earth3-Veg-LR historical-ssp585 (1)	1.2e+8 (3.3e+6 ... 7.2e+9)	1.6 (1.4 ... 1.7)
EC-Earth3-Veg historical-ssp585 (1)	1.2e+8 (3.4e+6 ... 6.9e+9)	1.8 (1.6 ... 1.9)
EC-Earth3 historical-ssp585 (1)	4.0e+7 (1.1e+6 ... 2.1e+9)	1.8 (1.6 ... 2.0)
GFDL-CM4 historical-ssp585 (1)	1.4e+15 (1.2e+12 ... 3.1e+18)	2.0 (1.8 ... 2.2)
GFDL-ESM4 historical-ssp585 (1)	1.4e+9 (1.2e+7 ... 2.7e+11)	1.4 (1.2 ... 1.6)
HadGEM3-GC31-LL historical-ssp585 (1)	4.8e+11 (3.1e+9 ... 2.3e+14)	1.9 (1.7 ... 2.0)
HadGEM3-GC31-MM historical-ssp585 (1)	2.2e+11 (1.5e+9 ... 8.7e+13)	2.0 (1.8 ... 2.2)
IITM-ESM historical-ssp585 (1)	4.0e+12 (1.3e+10 ... 2.5e+15)	1.5 (1.4 ... 1.7)
INM-CM4-8 historical-ssp585 (1)	1.1e+10 (9.1e+7 ... 2.8e+12)	1.6 (1.4 ... 1.7)
INM-CM5-0 historical-ssp585 (1)	3.0e+13 (6.4e+10 ... 4.2e+16)	1.8 (1.6 ... 1.9)
IPSL-CM6A-LR historical-ssp585 (1)	1.9e+11 (1.4e+9 ... 8.8e+13)	1.6 (1.5 ... 1.7)
KACE-1-0-G historical-ssp585 (1)	1.2e+10 (1.3e+8 ... 2.0e+12)	2.1 (2.0 ... 2.3)
MIROC-ES2L historical-ssp585 (1)	3.7e+10 (2.0e+8 ... 1.2e+13)	1.5 (1.3 ... 1.7)
MPI-ESM1-2-HR historical-ssp585 (1)	1.1e+16 (1.1e+13 ... 4.7e+19)	1.6 (1.5 ... 1.8)
MPI-ESM1-2-LR historical-ssp585 (1)	1275174008127252 (1.4e+12 ... 3.4e+18)	1.7 (1.6 ... 1.9)
MRI-ESM2-0 historical-ssp585 (1)	3.2e+10 (3.1e+8 ... 6.8e+12)	1.5 (1.4 ... 1.7)
NorESM2-LM historical-ssp585 (1)	4.3e+7 (1.1e+6 ... 4.8e+9)	1.9 (1.6 ... 2.2)
NorESM2-MM historical-ssp585 (1)	2.6e+7 (4.9e+5 ... 2.3e+9)	1.7 (1.4 ... 1.9)
TaiESM1 historical-ssp585 (1)	7.3e+11 (2.0e+9 ... 3.8e+14)	2.0 (1.8 ... 2.2)
UKESM1-0-LL historical-ssp585 (1)	1.8e+10 (2.2e+8 ... 3.4e+12)	1.9 (1.7 ... 2.1)
EC-EARTH3P HighResMIP (1)	2.5e+14 (1.5e+11 ... ∞)	1.6 (1.4 ... 1.8)
EC-EARTH3P-HR HighResMIP (1)	∞ (1.1e+15 ... ∞)	1.8 (1.6 ... 2.0)
HadGEM3-GC31-HM HighResMIP (1)	2.3e+14 (1.0e+11 ... ∞)	2.1 (1.9 ... 2.3)
HadGEM3-GC31-LM HighResMIP (1)	7.2e+13 (3.1e+10 ... ∞)	1.9 (1.7 ... 2.2)

HadGEM3-GC31-MM HighResMIP (1)	2.7e+15 (9.0e+11 ... ∞)	2.0 (1.7 ... 2.2)
CNRM-CM6-1 HighResMIP (1)	2.6e+14 (7.7e+10 ... ∞)	1.8 (1.6 ... 2.0)
CNRM-CM6-1-HR HighResMIP (1)	2.8e+14 (8.9e+10 ... ∞)	1.6 (1.4 ... 1.8)

Table A4. Probability Ratio (PR) and change in intensity of the 2022 **JJA average precipitation in the NHET region** between the current climate and the pre-industrial climate, from the observed datasets and the models that passed validation. This event is defined as a 1-in-10 year event based on observations.

Model / Observations	**Probability ratio PR [-]**	**Change in intensity ΔI [%]**
ERA5	1.4 (0.34 ... 6.6)	-0.65 (-2.9 ... 2.2)
	(...)	(...)
	(...)	(...)
AM2.5C360 amip1871-2021 (10)	0.26 (0.18 ... 0.36)	3.0 (2.3 ... 3.7)
ACCESS-CM2 ()	1.0 (0.46 ... 1.7)	-0.39 (-5.3 ... 5.8)
ACCESS-ESM1-5 ()	1.2 (0.64 ... 2.1)	-1.9 (-9.9 ... 5.0)
BCC-CSM2-MR ()	1.6 (0.82 ... 2.8)	-6.2 (-13 ... 2.2)
CESM2-WACCM ()	1.4 (0.72 ... 2.3)	-2.8 (-7.8 ... 2.6)
CESM2 ()	2.4 (1.2 ... 4.2)	-9.3 (-17 ... -1.6)
CMCC-CM2-SR5 ()	2.0 (1.2 ... 3.0)	-8.3 (-14 ... -2.1)
CMCC-ESM2 ()	2.0 (1.0 ... 3.3)	-8.1 (-14 ... -0.53)
CNRM-CM6-1-HR ()	1.1 (0.64 ... 1.8)	-0.91 (-8.9 ... 5.6)
CNRM-CM6-1 ()	0.82 (0.45 ... 1.3)	2.6 (-4.2 ... 9.6)
CNRM-ESM2-1 ()	1.8 (0.99 ... 3.1)	-7.9 (-16 ... 0.17)
CanESM5 ()	1.6 (0.89 ... 2.5)	-4.0 (-8.0 ... 0.86)
EC-Earth3-CC ()	0.44 (0.27 ... 0.65)	8.2 (4.7 ... 12)
EC-Earth3-Veg-LR ()	0.51 (0.24 ... 0.87)	7.6 (1.7 ... 14)
EC-Earth3-Veg ()	0.89 (0.57 ... 1.3)	1.4 (-3.0 ... 6.2)
EC-Earth3 ()	0.60 (0.31 ... 0.98)	5.5 (0.30 ... 11)
GFDL-CM4 ()	1.2 (0.50 ... 2.0)	-1.1 (-5.5 ... 4.7)
GFDL-ESM4 ()	2.0 (0.97 ... 4.7)	-5.7 (-13 ... 0.19)
HadGEM3-GC31-LL ()	3.8 (2.0 ... 7.5)	-12 (-18 ... -5.8)
HadGEM3-GC31-MM ()	4.6 (2.3 ... 9.1)	-15 (-22 ... -8.0)
INM-CM5-0 ()	4.0 (2.2 ... 7.0)	-22 (-29 ... -12)
MIROC6 ()	0.31 (0.12 ... 0.50)	11 (6.6 ... 17)
MPI-ESM1-2-HR ()	2.6 (1.3 ... 4.5)	-9.7 (-15 ... -2.7)

MPI-ESM1-2-LR ()	8.9 (3.8 ... 20)	-18 (-25 ... -11)
MRI-ESM2-0 ()	0.60 (0.25 ... 1.2)	3.8 (-1.5 ... 8.9)
NorESM2-LM ()	3.8 (1.5 ... 6.7)	-16 (-25 ... -5.3)
NorESM2-MM ()	1.9 (1.0 ... 3.1)	-7.7 (-14 ... 0.022)
TaiESM1 ()	3.2 (1.4 ... 5.7)	-13 (-21 ... -4.3)
UKESM1-0-LL ()	1.8 (0.98 ... 3.0)	-7.1 (-14 ... 0.23)
EC-EARTH3P-HR ()	0.32 (0.070 ... 1.3)	2.2 (-0.51 ... 4.7)
HadGEM3-GC31-HM ()	0.25 (0.064 ... 0.65)	3.1 (0.90 ... 5.4)
HadGEM3-GC31-LM ()	0.27 (0.077 ... 0.80)	3.1 (0.53 ... 5.6)
HadGEM3-GC31-MM ()	0.30 (0.081 ... 0.83)	2.9 (0.49 ... 5.5)
CNRM-CM6-1 ()	0.88 (0.21 ... 3.7)	0.28 (-2.7 ... 3.2)
CNRM-CM6-1-HR ()	0.47 (0.098 ... 1.9)	1.5 (-1.3 ... 4.2)

References

All references are hyperlinked in the main text